Co-seismic deformation of deep slabs based on summed CMT data

Iain W. Bailey,[1] Lisa A. Alpert,[1] Thorsten W. Becker,[1] and Meghan S. Miller[1]

Received 18 October 2011; revised 14 February 2012; accepted 23 February 2012; published 14 April 2012.

[1] We assess the co-seismic deformation inferred from earthquake moment tensor solutions for subducting slabs at depths greater than 50 km globally. We rotate each moment tensor into a local slab reference frame, then sum tensors within 50 km depth bins to approximate long term deformation characteristics. This builds upon previous analyses by using the up-to-date global Centroid Moment Tensor catalog, incorporating a more complete slab geometry, and focusing on the 3-D aspects of slab deformation. Results show a general consistency with Isacks and Molnar (1969), who found that most slabs can be divided into intermediate-extensional, intermediate-extensional-deep-compressional, and intermediate to deep-compressional categories. Exceptions to these three categories can be related to slab bending in the top 100 km, plate convergence that is oblique to the trench normal direction, and regions of higher focal mechanism heterogeneity. The regions of higher focal mechanism heterogeneity appear where there are along-strike changes in slab geometry and/or evidence of double-seismic zones. We find that the sense of deformation in the intermediate strain axis direction is opposite to that of the down-dip direction, in agreement with Kuge and Kawakatsu (1993). By quantitative comparison to numerical models of global mantle flow, we show that these observations are consistent with deformation of viscous slabs responding to their own negative buoyancy and an upper to lower mantle viscosity increase.

Citation: Bailey, I. W., L. A. Alpert, T. W. Becker, and M. S. Miller (2012), Co-seismic deformation of deep slabs based on summed CMT data, *J. Geophys. Res.*, *117*, B04404, doi:10.1029/2011JB008943.

1. Introduction

[2] The interpretation of deep earthquakes as evidence for descending slabs of cold lithosphere was key to the development of plate tectonic theory [e.g., *Sykes*, 1966; *Isacks et al.*, 1968]. The orientation of focal mechanisms corresponding to these earthquakes relate to the deviatoric stress conditions associated with the subducting slabs. As such, they provide constraints on a range of problems such as the relative role of slab pull in driving plate motion, the viscosity structure of the mantle and the strength of slabs [e.g., *Forsyth and Uyeda*, 1975; *Vassiliou and Hager*, 1988; *Billen and Gurnis*, 2003; *Conrad and Lithgow-Bertelloni*, 2004; *Alisic et al.*, 2010; *Alpert et al.*, 2010]. In two key studies, *Isacks and Molnar* [1969, 1971] analyzed the orientation of deep earthquake focal mechanisms globally. They observed that either the compressional (P) or tensional (T) axis of a focal mechanism tends to align with the down-dip direction of the slab as inferred from the earthquake locations. From a visual inspection of which axis was predominantly down-dip, *Isacks and Molnar* [1971] categorized different depth sections of 24 slabs as compressive, extensive or unclear, leading to the following generalizations: (1) Intermediate depth earthquakes ($100 \lesssim z \lesssim 300$ km where z is depth) in slabs where there are no deep earthquakes are generally down-dip extensional. (2) Deep ($300 \lesssim z \lesssim 700$ km) earthquakes are nearly always down-dip compressional. (3) Where there is a gap or sparse seismicity between intermediate and deep earthquakes, the intermediate depth earthquakes are generally down-dip extensional. (4) Where the seismicity is continuous with depth to $z \gtrsim 300$ km, the intermediate depth earthquakes are generally down-dip compressional.

[3] The interpretation of the first observation is that the negative buoyancy of the cold dense slab leads to tensile stresses in its shallower parts. The second observation is interpreted as the effect of the slab reaching the higher viscosity lower mantle at $z \approx 660$ km such that it becomes supported from below. The third observation is interpreted as a combination of these two effects while the fourth indicates that the slab has become fully supported from below after extended contact with the lower mantle. Two dimensional modeling [*Vassiliou and Hager*, 1988] reproduced the pattern of extension at intermediate depths due to gravitational sinking of a viscous slab, with deeper compression dominantly controlled by proximity to a viscosity increase from upper to lower mantle. *Alpert et al.* [2010] reproduced these two effects simultaneously in multiple slabs for a 3-D global flow model that incorporated radial and lateral viscosity variations.

[4] Studies subsequent to *Isacks and Molnar* [1971] have shown that P or T axes tend to point down-dip using more quantitative analyses of orientations and larger focal mechanism data sets [e.g., *Apperson and Frohlich*, 1987;

[1]Department of Earth Sciences, University of Southern California, Los Angeles, California, USA.

0148-0227/12/2011JB008943

Vassiliou and Hager, 1988; *Chen et al.*, 2004; *Alpert et al.*, 2010]. While the first and second observations noted previously are supported by these studies, there is less consensus on the patterns of intermediate depth earthquakes for slabs with deep seismicity. Other factors suggested to influence focal mechanism orientations include slab bending and unbending [e.g., *Engdahl and Scholz*, 1977], the interaction between subduction rate and slab age [*Fujita and Kanamori*, 1981], shearing effects of mantle flow [*Giardini and Woodhouse*, 1986], unlocking at the slab interface by mega-thrust earthquakes [*Astiz et al.*, 1988], fossil fault orientations [*Jiao et al.*, 2000] and the angle of slab dip [*Brudzinski and Chen*, 2005]. The four main observations of *Isacks and Molnar* [1971] predict three "Isacks and Molnar categories" of slab: intermediate extension (IE) type, intermediate extension-deep compression (IE-DC) type, and intermediate compression-deep compression (IC-DC) type. The question of whether other factors can lead to exceptions from these categories was approached by *Chen et al.* [2004], who analyzed intermediate depth earthquake focal mechanisms globally and concluded that while the Isacks and Molnar categories explained more of the data than any other model, arc curvature and an interaction between slab age and mantle phase transitions can lead to exceptions.

[5] Here, we focus on how well the orientation of focal mechanisms for slab earthquakes are explained by these three slab categories and whether other effects can lead to exceptions. We expand on the analysis of *Chen et al.* [2004] by increasing the earthquake data set numerically and geographically, by incorporating improved representation of slab geometry, by focusing in more detail on the 3-D aspects of slab deformation, and by comparison with numerical modeling results. Slab geometry is important for several of the factors listed previously as suggested influences on co-seismic deformation. We use the Regionalized Upper Mantle (RUM) slab contours [*Gudmundsson and Sambridge*, 1998] to obtain greater coverage of slabs than in previous studies, allowing us to assess the role of slab geometry on co-seismic deformation in more detail.

[6] The Isacks and Molnar slab categories are based on the nature of deformation in the down-dip direction of the slab, and hence do not incorporate 3-D aspects of slab deformation fully. To understand 3-D aspects of co-seismic deformation in more detail requires going beyond the double-couple representation used previously [*Isacks and Molnar*, 1971; *Apperson and Frohlich*, 1987; *Chen et al.*, 2004]. Departure from a double-couple mechanism can be quantified by the intermediate eigenvalue of the moment tensor, reflecting non-zero strain in the B-axis direction, which can provide clues as to the rheological controls on slab deformation. For example, large extensional intermediate strain perpendicular to a down-dip P-axis indicates that the slab is extending as much in the slab-normal as the along-strike direction. This would imply that any stiffness of the slab has little effect on resisting deformation along-strike. Departures from a double-couple mechanism are often referred to in terms of the relative size and sign of a compensated linear vector dipole (CLVD) component [e.g., *Knopoff and Randall*, 1970; *Julian et al.*, 1998], and have been previously assessed in relation to deep earthquakes by, e.g., *Giardini* [1984], *Kuge and Kawakatsu* [1993], and *Frohlich* [1995]. *Giardini* [1984] showed systematic changes in the CLVD components related to earthquake depths and suggested a relation to the observations of *Isacks and Molnar* [1971]. *Kuge and Kawakatsu* [1993] assessed this more quantitatively and showed a relation between the average CLVD component properties in a slab and the ratio of in-plate compression to in-plate extension earthquakes. They found that a greater proportion of P-axes close to the plane of the slab corresponded to generally extensive strain in the B-axis directions, while a greater proportion of T-axes closer to the slab plane corresponded to generally compressive strain in the B-axis directions. The same correlation is reproduced by *Frohlich* [2006] for the data set used by *Apperson and Frohlich* [1987].

[7] Interpretation of variations in CLVD size and orientation for deep earthquake focal mechanisms requires a 3-D understanding of slabs. *Frohlich* [1995] suggested interpretations relating to extensive or compressive forces produced by slab bending, but pointed out that there is no unique interpretation of a given CLVD component in this way. *Kuge and Kawakatsu* [1993] showed evidence that CLVD components can be related to sub-events with varying orientations but with the principal axis in the down-dip direction remaining relatively stable. However, they also showed that CLVD components may result from a double-couple radiation pattern modified by the high velocity slab. This highlights a problem with analysis of CLVD components in that it relies on moment tensor inversions constraining the value of the smallest absolute strain. In this study, we assess the CLVD components of summed moment tensors which, although affected by the CLVD components of individual moment tensors, are dominated by variation in the better constrained P and T axes orientations [e.g., *Bailey et al.*, 2010]. Such variation is likely to reflect persistent characteristics of the regional loading stress. We show that CLVD patterns in summed moment tensors generally conform to the patterns observed in individual moment tensors by *Kuge and Kawakatsu* [1993]. We aid our interpretation of observed CLVD patterns by comparison to recent numerical model results [*Alpert et al.*, 2010] that fully incorporate 3-D effects and the interaction between different slabs. *Alpert et al.* [2010] quantified the model predictions of stress within slabs by the average fit of predicted to observed P-axis orientations. Here, we target the CLVD characteristics in the model results to better understand the 3-D aspects of slab stresses. These comparisons highlight that the general CLVD patterns in CMT data can be related to viscous behavior of slabs in addition to the interaction of the slab geometry with surrounding mantle flow.

2. Data and Methods

2.1. Moment Tensor and Slab Geometry Data

[8] We use the global Centroid Moment Tensor (CMT) catalog [*Dziewonski et al.*, 1981; *Dziewonski and Woodhouse*, 1983] (http://www.globalcmt.org/, accessed June 2011) to obtain focal mechanisms of earthquakes occurring between 1976 and 2010 inclusive. The catalog represents earthquakes as point-source, symmetric and deviatoric moment tensors, computed by inversion of body wave, surface wave and sometimes normal mode data [*Ekström*, 2007]. Events with depth $z \leq 50$ km are removed. We estimate the moment magnitude M_W of completeness for the remaining data to be

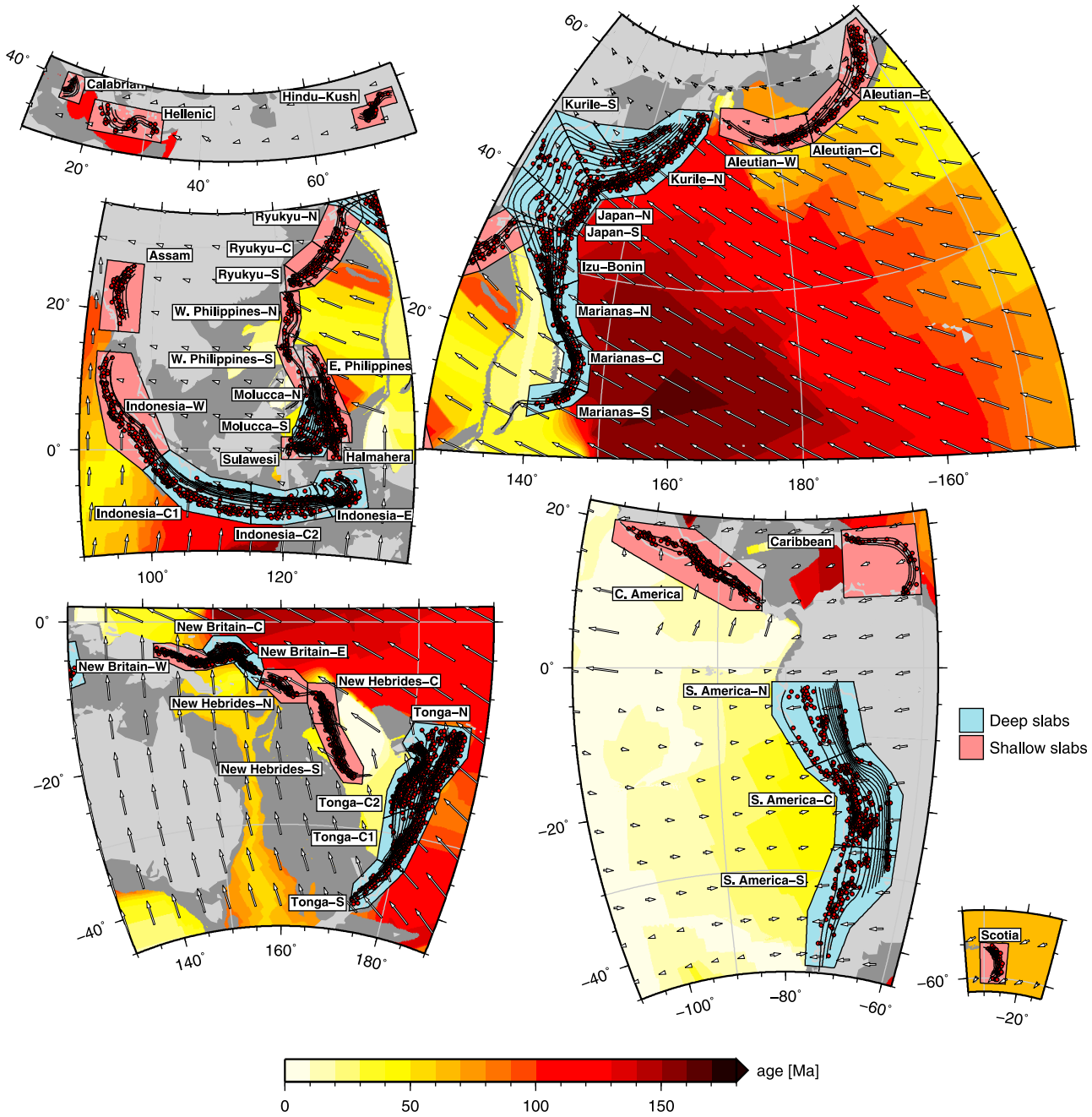

Figure 1. Locations of slabs and CMT data used in this study together with seafloor ages [*Müller et al.*, 2008] and plate motion vectors from the NUVEL-HS3 [*Gripp and Gordon*, 2002] model. Black lines show the 50 km depth interval slab contours of *Gudmundsson and Sambridge* [1998] which overlay red circles showing the CMT centroid locations. Colored polygons and associated labels show the slab regions defined for this study, with red and blue indicating whether the slab regions are classified as shallow or deep, respectively.

~5.2 based on a visual inspection of the M_W histogram. Since the results presented here are similar when including or omitting CMTs with $M_W < 5.2$, we infer that there is no strong bias toward certain mechanism types below the completeness threshold and use the entire magnitude range for our analysis.

[9] To define slab geometry we use the RUM slab contours [*Gudmundsson and Sambridge*, 1998], which have a 50 km depth interval and were created by fitting a surface to the top of seismicity for 24 separate slabs using relocated hypocenter data. We do not incorporate two of their smallest slab surfaces (Luzon and Mindanao) where there are no contours defined below 150 km. The remaining slabs are subdivided into 45 slab regions (Figure 1) which were initially defined to enclose similarly sized areas while containing sufficient CMT data and minimal changes in slab geometry. Subsequent, iterative adjustments were made to separate distinct co-seismic deformation patterns. The

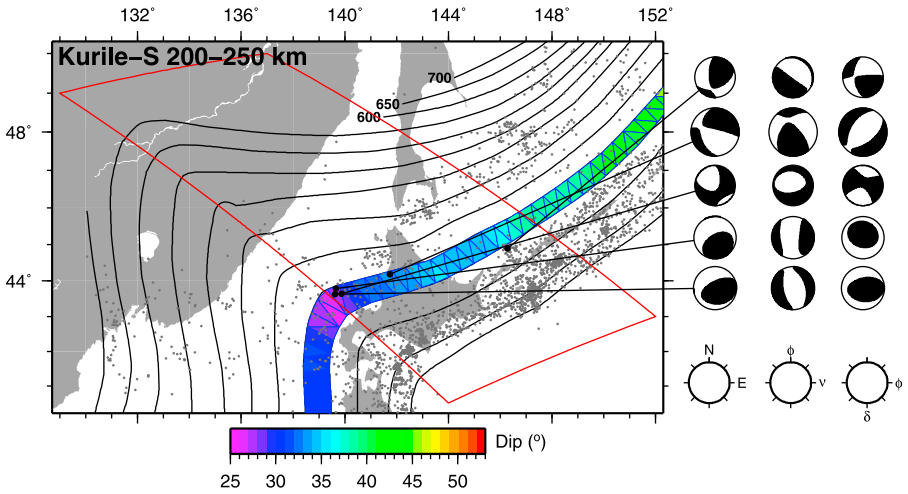

Figure 2. Example slab contours, triangulation and CMT rotation applied to the $200 < z \leq 250$ km depth range of the Kurile-S slab. Re-sampled points on the slab contours (black lines) are triangulated to obtain slab patches which have unique strike and dip values. Five example CMTs from within the depth range are associated with the slab triangles that have the closest midpoints. Beach balls show the CMT orientations before and after two rotations into the slab coordinate system, where ϕ, ν and δ indicate the along-strike, slab-normal and down-dip directions. The first rotation shows the beach balls as looking down-dip into the slab and the second (right-most column) shows the view used in subsequent figures, looking away from the slab-normal. Red lines show the extent of the polygon used to define this particular slab region. Gray dots show the epicenters from the EHB catalog [*Engdahl et al.*, 1998] for earthquakes within a $50 < z \leq 700$ depth range.

naming of the sub-regions generally follows *Gudmundsson and Sambridge* [1998] except in cases where other names are perceived to be more conventional. Slab regions are categorized as "deep" if the deepest slab contour is below 350 km and "shallow" otherwise (Figure 1).

[10] From a ~50 km discretization of the slab contours, we project the longitude and latitude of points on adjacent contours to a 2-D Cartesian coordinate system and triangulate between those points. After projecting back into geographical coordinates, each triangle is assigned a strike, dip and center location based its vertices. We associate CMTs with the nearest slab if their centroid is within 75 km of a triangle's center and within 50 km distance normal to that triangle. This results in a data set of 7, 071 slab-associated CMTs (Figure 1) accounting for 81% of the catalog in this depth range. We rotate the CMTs into a right-handed slab coordinate system (updip $\hat{\delta}$, upward pointing slab-normal $\hat{\nu}$, along-strike $\hat{\phi}$) based on the strikes and dips of the closest triangle. An example showing the calculated triangle patches and rotation of five CMTs in the $200 < z \leq 250$ depth range for the Kurile-S slab region is given in Figure 2.

2.2. Moment Tensor Summations

[11] We characterize co-seismic deformation by summing moment tensors:

$$\mathbf{M}^{\Sigma} = \sum_{k=1}^{N} \mathbf{M}_k, \tag{1}$$

where $\mathbf{M}_k$ is the k^{th} moment tensor in a population of size N. Assuming homogeneous isotropic elastic properties for an arbitrary volume containing the earthquakes, $\mathbf{M}^{\Sigma}$ relates to the co-seismic strain of that volume by a constant scaling factor [*Kostrov*, 1974]. In our case we sum tensors after rotation into the slab reference frame and the implied strain therefore represents co-seismic deformation of the slab in a $\hat{\delta} - \hat{\nu} - \hat{\phi}$ coordinate system. The scalar moment of $\mathbf{M}^{\Sigma}$ is $M_0 = \|\mathbf{M}^{\Sigma}\| / \sqrt{2}$, where $\|\mathbf{M}_k\|$ is the Euclidean Norm of $\mathbf{M}_k$, and we estimate a moment magnitude M_W using the relation of *Hanks and Kanamori* [1979]. M_0 for a summed tensor is generally smaller than the cumulative moment release for the population since tensors with varying orientations cancel each other out to some extent. Since $\mathbf{M}^{\Sigma}$ can be dominated by the largest earthquake in a population, we also consider the average source mechanism tensor [e.g., *Riedesel and Jordan*, 1989; *Bailey et al.*, 2009]:

$$\widehat{\mathbf{M}}^{\Sigma} = \frac{1}{N} \sum_{k=1}^{N} \widehat{\mathbf{M}}_k = \frac{1}{N} \sum_{k=1}^{N} \frac{\mathbf{M}_k}{\|\mathbf{M}_k\|}. \tag{2}$$

[12] The average source mechanism tensor can be thought of as the mean moment tensor orientation, though orientation in this case refers to a 6-D unit vector describing the symmetric moment tensor and incorporating changes in the relative sizes of the three principal strains. This tensor summation is dominated by smaller earthquakes due to the Gutenberg-Richter law distribution of earthquake magnitudes. Similarity of the principal axes orientations for $\mathbf{M}^{\Sigma}$ over a range of magnitude scales [e.g., *Amelung and King*, 1997; *Bailey et al.*, 2009] often leads to similar results for $\widehat{\mathbf{M}}^{\Sigma}$ and $\mathbf{M}^{\Sigma}$. This suggests a similar response of small and large earthquakes to a single loading stress orientation acting upon the same faulting structures. Following *Frohlich and Apperson* [1992] and *Bailey et al.* [2010], we use $\|\widehat{\mathbf{M}}^{\Sigma}\|$, which lies between 0 and 1, to measure the consistency in

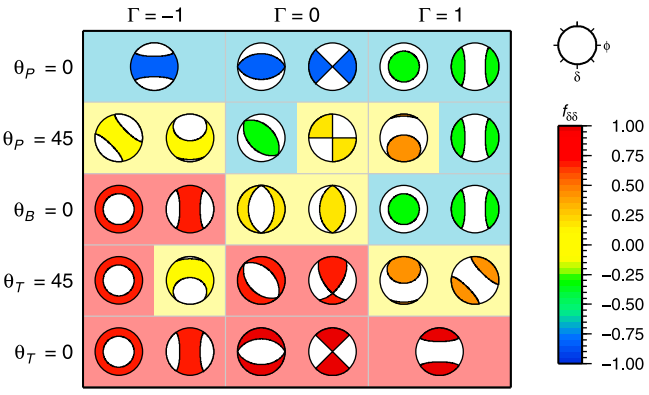

Figure 3. Example deviatoric moment tensor orientations shown by beach ball representations and associated values of relative CLVD component size Γ, principal axis inclination with respect to the down-dip axis, θ, and relative down-dip moment $f_{\delta\delta}$ (color of the extensional region). The coordinate system is such that the down-dip direction points toward to bottom of the page. Classification of the orientation as either down-dip compressional, extensional or oblique is illustrated in each case by a light blue, red or yellow background, respectively.

moment tensor orientations for the population considered. For a uniformly distributed random population of deviatoric tensor orientations, the expected value of $\|\widehat{\mathbf{M}}^{\Sigma}\|$ is $1/\sqrt{N}$, which is useful to calculate when comparing $\|\widehat{\mathbf{M}}^{\Sigma}\|$ for different sized populations.

[13] We compute $\mathbf{M}^{\Sigma}$ and $\widehat{\mathbf{M}}^{\Sigma}$ for the rotated CMTs in 50 km depth bins for our global data set of slab associated CMTs, and again for each of the 45 slab regions, though $\widehat{\mathbf{M}}^{\Sigma}$ is only computed for bins containing at least three CMTs. In order to simplify the presentation of our main results, we focus on $\widehat{\mathbf{M}}^{\Sigma}$ when considering subregions in section 3. This is adequate since the orientations of $\mathbf{M}^{\Sigma}$ and $\widehat{\mathbf{M}}^{\Sigma}$ are generally consistent in the same bins, and analysis of $\|\widehat{\mathbf{M}}^{\Sigma}\|$ carries information about consistency of orientations. Other summation results are presented in the auxiliary material.[1] In all cases, we display summation results using beach ball representations, where the down-dip direction points toward the bottom of the page, along-strike points to the right, and slab-normal points out of the page.

2.3. Analysis Quantities

[14] We interpret each $\mathbf{M}^{\Sigma}$ and $\widehat{\mathbf{M}}^{\Sigma}$ in terms of its down-dip deformation state, orientation of the principal axis closest to down-dip and the size of the CLVD component using three scalar quantities. The down-dip deformation state is quantified by

$$f_{\delta\delta} = \frac{m_{\delta\delta}}{\max(-\lambda_1, \lambda_3)}, \tag{3}$$

where $m_{\delta\delta}$ denotes the down-dip component of $\mathbf{M}^{\Sigma}$ or $\widehat{\mathbf{M}}^{\Sigma}$, and λ_1 and λ_3 denote the minimum and maximum eigenvalues, respectively, of $\mathbf{M}^{\Sigma}$ or $\widehat{\mathbf{M}}^{\Sigma}$. The value of $f_{\delta\delta}$ quantifies the compressive (negative) or extensive (positive) down-dip moment relative to the moment in the direction of the dominant axis of the tensor, and ranges from -1 to 1. This incorporates extension or compression that may result from a tensor with a CLVD component and a B-axis close to the down-dip direction. We calculate $f_{\delta\delta}$ for all $\mathbf{M}^{\Sigma}$ and $\widehat{\mathbf{M}}^{\Sigma}$, then interpret the result as down-dip compressional if $f_{\delta\delta} < -0.45$, down-dip extension if $f_{\delta\delta} > 0.45$, and oblique otherwise. This classification is used to assess the agreement of summed tensors with the Isacks and Molnar categories, and is illustrated in Figure 3. The value of 0.45 is chosen so it is small enough for CLVD components to influence the interpretation of the deformation state, while being large enough that it reflects the orientation of the P and T axes in the case of double-couple mechanisms. For a randomly oriented moment tensor population, ~60% would be interpreted as oblique based on this threshold.

[15] To quantify the distinction between IE-DC and IC-DC categories, we estimate the depth of change from extension to compression, z_c, by fitting two lines with $f_{\delta\delta} = 1$ and $f_{\delta\delta} = -1$ to the bin values of $f_{\delta\delta}$ in each deep-type slab region. We use $z_c \leq 100$ km to define the IC-DC category slab regions. Based on the conclusions of *Isacks and Molnar* [1971], we expect z_c to coincide with a depth range where there is sparse seismicity. To test this, we associate hypocenter data from the EHB catalog [*Engdahl et al.*, 1998] (http://www.isc.ac.uk) with the slab regions based on the same distance criteria as for the CMTs. We then compute the number of above completeness hypocenters in 50 km depth bins for each slab region, where magnitude of completeness is estimated by visual assessment of the magnitude-frequency distribution for the region. In cases where there is one or more bin with no earthquakes above bins with earthquakes, we define the seismicity-based z_c estimate as the bin boundary closest to the center of the seismicity gap. Elsewhere, we use the bottom of the bin with the lowest number of earthquakes, with the condition that the underlying bin has more earthquakes. To prevent sparse seismicity at the tip of the slabs influencing this estimate, we restrict the possible depths of z_c to $z \leq 450$ km.

[16] Following Frohlich [1995] and *Kagan* [2009], we quantify the relative size of the CLVD component by

$$\Gamma = \frac{3\sqrt{6}\det(\mathbf{M})}{\|\mathbf{M}\|^3}, \tag{4}$$

where $\mathbf{M}$ denotes the moment tensor for a single CMT and det($\mathbf{M}$) denotes its determinant. $\Gamma = -1$ corresponds to uniaxial compression, $\Gamma = 1$ corresponds to uniaxial extension, and $\Gamma = 0$ corresponds to a pure double-couple mechanism. $\mathbf{M}$ can be substituted by $\mathbf{M}^{\Sigma}$ or $\widehat{\mathbf{M}}^{\Sigma}$ to quantify the CLVD components of the summed tensors. In $\mathbf{M}^{\Sigma}$ and $\widehat{\mathbf{M}}^{\Sigma}$, non-zero values of Γ may result from CLVD components in the CMT population or from rotationally asymmetric variation of the principal axes among the population [e.g., *Frohlich*, 1995; *Kagan*, 2009; *Bailey et al.*, 2010]. For example, a negative value of Γ can indicate either compressive strains in the B-axis direction for a number of near-homogeneously oriented earthquakes, or that the T-axis has a relatively stable orientation within the population while the

[1] Auxiliary materials are available in the HTML. doi:10.1029/2011JB008943.

Table 1. Key Viscosity Variations in the Six Model Setups Presented in This Paper[a]

Name	η_{LM}/η_{UM}	η_L/η_{UM}	η_A/η_{UM}
Control	30	10	1
No upper/lower mantle η contrast	1	10	1
Weak slab	30	1	1
Stiff slab	30	100	1
Extra stiff slab	30	1000	1
Weak asthenosphere layer	30	10	0.1

[a]Upper mantle background viscosity η_{UM} defines the reference viscosity. The viscosities η_L, η_{LM} and η_A denote the viscosities of the slab, lower mantle and asthenosphere, respectively.

P and B axes tend to interchange. The advantage of using Γ over $\varepsilon = \lambda_2/\max(-\lambda_1, \lambda_3)$ [e.g., *Giardini*, 1984; *Kuge and Kawakatsu*, 1993] is that Γ has a uniform distribution for randomly selected deviatoric tensor orientations, making it easier to quantify deviations from random [*Kagan*, 2009].

[17] The value of Γ is not independent of $f_{\delta\delta}$, and hence $f_{\delta\delta}$ is not a good measure with which to assess the orientation of CLVD components with respect to the slab. To incorporate the CLVD orientation into our analysis we investigate the CLVD patterns in relation to the slab deformation state by plotting Γ as a function of the angle θ between the P, T or B axis and the down-dip direction, depending on whichever is smallest. Plotting of Γ versus θ is analogous to *Kuge and Kawakatsu* [1993, Figure 2] and *Frohlich* [2006, Figure 6.30]. The difference is that those authors plot average ε (equivalent to Γ) versus proportion of compressive to extensive events for each slab, while we plot Γ and the degree of compression/extension for each tensor. Our approach allows us to compare CLVD characteristics for individual CMTs and for the summed tensors, as well as being less sensitive to choices made during data selection. Since the relationship between $f_{\delta\delta}$, θ and Γ can be counterintuitive, beach ball representations of example moment tensors and their associated values are shown in Figure 3.

2.4. Global Flow Model Comparisons

[18] The numerical modeling results used to interpret tensor summation results in terms of slab stresses are taken directly from the study of *Alpert et al.* [2010], where the modeling approach is described in detail. This approach employs CitcomS [*Zhong et al.*, 2000] to solve for Stokes' flow and associated stress due to an imposed viscosity and density structure in the Boussinesq approximation, arriving at an instantaneous solution for global mantle flow. Radial viscosity structure is defined by a lithosphere with viscosity η_L, asthenosphere ($100 < z \leq 300$ km) with viscosity η_A, upper mantle ($300 < z \leq 660$ km) with viscosity η_{UM} and lower mantle ($660 < z \leq 2,891$ km) with viscosity η_{LM}. Slabs are incorporated by converting the RUM slabs into constant thickness temperature and density anomalies relative to the upper mantle. These temperature anomalies are translated into viscosity anomalies such that the maximum slab viscosity is the same as η_L. *Alpert et al.* [2010] investigated the effect of a range of parameters on the intraslab stresses using a total of 226 models. We select a subset of six models by choosing a well performing, simple parameter setup as a control case and adjusting one of the viscosity parameters η_L, η_A and η_{LM}, in each of the other five. All viscosities are related to the upper mantle reference viscosity $\eta_{UM} = 10^{21}$ Pa s by constant factors. For the control model $\eta_L = 10\eta_{UM}$, $\eta_A = \eta_{UM}$ and $\eta_{LM} = 30\eta_{UM}$. For the other five models, factors are given in Table 1, along with names used to refer to the models in subsequent sections. The lithosphere and slab thickness is 100 km with a slab density anomaly of 3.9% in all models. Surface boundary conditions are prescribed plate motions from the NUVEL-HS3 model of *Gripp and Gordon* [2002] and we use a no-slip Core-Mantle Boundary (CMB) condition to induce net rotation related shearing. Fixing the CMB and prescribing absolute plate motion models channels the net rotation flow into the upper mantle [*Conrad and Behn*, 2010], roughly consistent with the dynamically induced net rotations from geodynamic models [*Zhong*, 2001; *Becker*, 2006].

[19] Stress results are extracted at the locations closest to each CMT and rotated as for the data. The model grid element spacing is 17 km which is the same order of magnitude as the CMT location uncertainty. We apply the slab region and depth binning to these CMT-associated stress results, then compute the average source mechanism tensor using equation (2) by substituting the deviatoric component of the model stress for $\mathbf{M}_k$. The binning removes some of the bias toward regions of abundant seismicity that is present in a global analysis. We compare average source mechanism tensor results because they appear spatially smoother and probably better reflect the long term stress behavior. By comparing the model deviatoric stresses with CMT orientations, we are assuming both that the CMTs represent the co-seismic strain and that the co-seismic strain represents an unbiased response to the loading stress. Both assumptions are justified if there is little anisotropy in the mechanical properties of the slab, and we have little basis for assuming otherwise. We assess the broad features of co-seismic slab deformation as a function of depth for the model by taking the average among the slab region bin values of $f_{\delta\delta}$ (equation (3)) and Γ (equation (4)). To place these results in the context of the Isacks and Molnar categories, we perform the averaging separately for the IE, IE-DC and IC-DC categories, where the sub-region category is assigned according to the $\widehat{\mathbf{M}}^{\Sigma}$ results of the CMT analysis.

[20] The model performance is quantified by comparing the orientation and CLVD components of the average source mechanism tensors via two separate quantities. The average difference in tensor orientation for the CMT $\widehat{\mathbf{M}}^{\Sigma}$ and model $\widehat{\mathbf{M}}^{\Sigma}_{mod}$ results is quantified by

$$\Theta^{DC} = \arccos\left[\left\langle \frac{\left(\widehat{\mathbf{M}}^{\Sigma}\right)^{DC}}{\left\|\left(\widehat{\mathbf{M}}^{\Sigma}\right)^{DC}\right\|} : \frac{\left(\widehat{\mathbf{M}}^{\Sigma}_{mod}\right)^{DC}}{\left\|\left(\widehat{\mathbf{M}}^{\Sigma}_{mod}\right)^{DC}\right\|} \right\rangle\right], \qquad (5)$$

where : indicates the tensor dot product, ^{DC} indicates the double-couple component (i.e., taking out the part with a non-zero intermediate eigenvalue), and the angular brackets indicate the average over all bins with three or more CMT data. Values of $\Theta^{DC} = 0°$, 90° and 180° indicate that the principal strain axes are parallel, orthogonal and opposite, respectively. For two populations of randomly oriented tensors, the expected mean and median values of Θ^{DC} would be 90°. We compare the model and data CLVD components

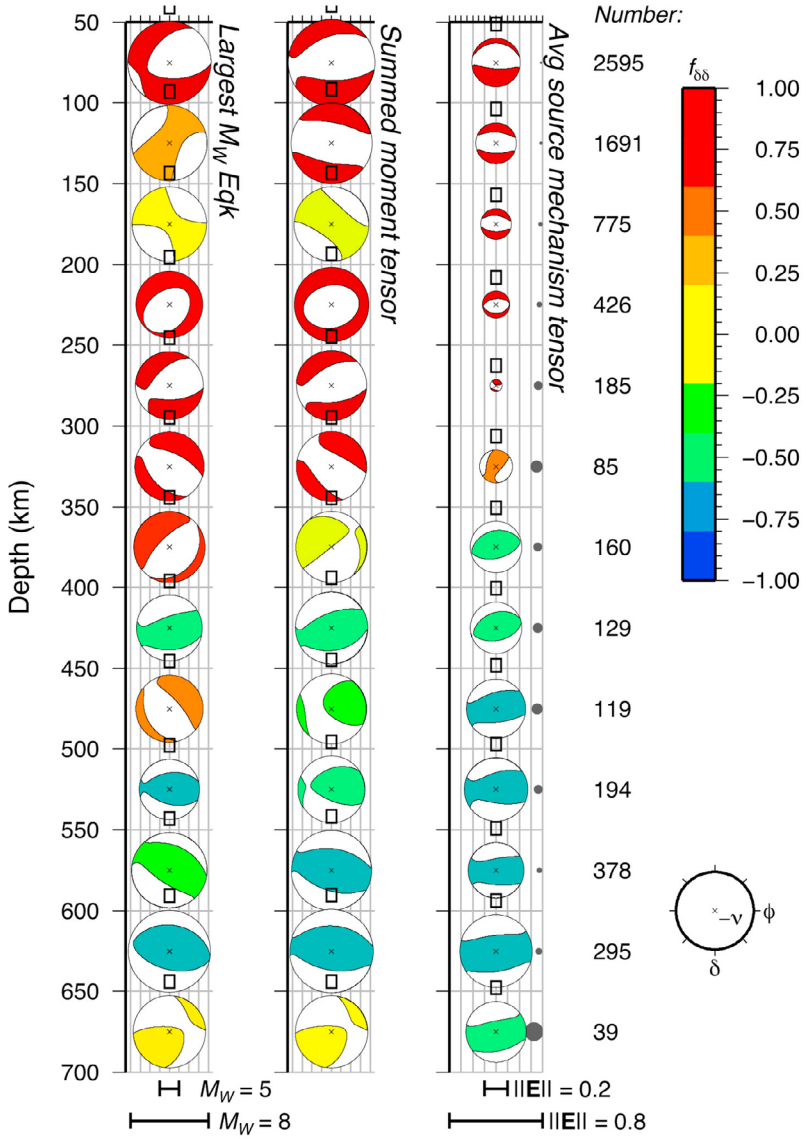

Figure 4. Beach ball representations of the largest earthquake CMTs, summed moment tensors $\mathbf{M}^{\Sigma}$, and average source mechanism tensors $\widehat{\mathbf{M}}^{\Sigma}$ in 50 km depth bins of slab earthquakes after rotation into a local slab coordinate system. The coordinate system (indicated in the bottom right) is plotted such that the down-dip direction points to the bottom of the page, and the cross overlaying each beach ball points opposite to the slab-normal. Unfilled and filled parts of the beach balls represent the orientation of compressive and extensive co-seismic strains, respectively. The colors of filled parts denote the size of the down-dip co-seismic deformation relative to the absolute maximum eigenvalue of the tensor. The radius of the beach balls for the largest event CMTs and $\mathbf{M}^{\Sigma}$ are scaled by the moment magnitude M_W [*Hanks and Kanamori*, 1979]. For $\widehat{\mathbf{M}}^{\Sigma}$, the radius indicates the consistency of orientations among the summed population. Gray circles adjacent to the $\widehat{\mathbf{M}}^{\Sigma}$ beach balls reflect the radius corresponding to the expected consistency for the same number of deviatoric tensors sampled from a uniform distribution.

based on the absolute difference in Γ for the average source mechanism tensors:

$$d\Gamma = \langle |\Gamma_{data} - \Gamma_{mod}| \rangle, \tag{6}$$

where Γ_{data} denotes Γ (equation (4)) for $\widehat{\mathbf{M}}^{\Sigma}$ from the CMT data, Γ_{mod} denotes Γ for $\widehat{\mathbf{M}}^{\Sigma}$ from the model stress tensors, and the angular brackets again indicate the average over all bins. For two populations of randomly oriented tensors, $d\Gamma$ follows a triangular distribution with a median of $2 - \sqrt{2} \approx 0.586$.

3. Results

3.1. Summed Moment Tensors for Global Depth Bins

[21] Summation results for the 50 km global depth bins in addition to the CMT for the largest event in each bin are shown in Figure 4. The dominant pattern throughout all

results is one of down-dip extension above $z \approx 350$ km and down-dip compression below. This is consistent with the Isacks and Molnar IE-DC category, though with a z_c of 350 km rather than 300 km. $\mathbf{M}^{\Sigma}$ shows very similar mechanisms to the largest earthquakes in each bin. This reflects the persistence of the Gutenberg-Richter distribution for the magnitudes of deep earthquake populations such that the largest earthquake in any population tends to release almost as much or more strain when compared to all other earthquakes combined. This effect is less evident where there are larger numbers of earthquakes, e.g., in the $50 < z \leq 150$ km bins, where greater sampling at the upper magnitude end of the Gutenberg-Richter distribution means that there are multiple large earthquakes.

[22] Comparison of results for $\mathbf{M}^{\Sigma}$ and $\widehat{\mathbf{M}}^{\Sigma}$ shows that changes in tensor orientation with depth are smoother for $\widehat{\mathbf{M}}^{\Sigma}$ than for $\mathbf{M}^{\Sigma}$. This suggests a smoothly varying stress field with depth that is better sampled by the more frequent small events than the less frequent and geographically separated large events. Deep bins show large CLVD components that indicate similar levels of extension within the plane of the along-strike and slab-normal directions. Nevertheless, there is a tendency for B-axes to be aligned with the along-strike direction indicating slightly greater extension in the slab-normal direction. There is a relative homogeneity of the CMT orientations within the bins below 350 km as quantified by $\|\widehat{\mathbf{M}}^{\Sigma}\|$. In contrast, the small beach balls for the intermediate depth range of 150–300 km show a low level of orientation consistency that is close to the expectation of a random set of moment tensor orientations.

3.2. Comparison of Slab Region Summed Tensors to Isacks and Molnar Categories

[23] Results for $\widehat{\mathbf{M}}^{\Sigma}$ computed over 50 km depth bins for 33 of the 45 slab regions are shown in Figure 5. We omit small slab regions or those with fewer depth bins from Figure 5 but these are included in the auxiliary material. For all slab regions, a total of 248 results for $\widehat{\mathbf{M}}^{\Sigma}$ were obtained based on the number of depth bins that contained at least three CMTs. This compares to 297 bins containing at least one CMT and 347 bins containing at least one EHB catalog hypocenter. We find that the results for $\mathbf{M}^{\Sigma}$ (auxiliary material) are generally consistent with results for $\widehat{\mathbf{M}}^{\Sigma}$ except where $\|\widehat{\mathbf{M}}^{\Sigma}\|$ is low, indicating a heterogeneous stress field. As for the global summation results and previous studies, we find that the majority of bins can be classified as either down-dip compressional or extensional. The pattern of down-dip extension above $z \approx 350$ km and compression below is generally reproduced at the slab region scale. In addition, the down-dip compression results tend to show extensional intermediate strain ($\Gamma < 0$) and down-dip extension results tend to show compressional intermediate strain ($\Gamma > 0$). These two observations are reproduced in the stresses from the numerical modeling for the control parameter setup (Figure 6).

[24] Examining the summation results in more detail, the percentage of bins classified as oblique is 26% for $\widehat{\mathbf{M}}^{\Sigma}$ and 32% for $\mathbf{M}^{\Sigma}$. Exceptions to the Isacks and Molnar categories can occur because of such oblique results or because the sense of deformation is opposite to that which is expected. The smallest proportion of exceptions are found for deep ($z > 350$ km) bins where down-dip compression dominates. For these bins, we find 20% disagreement with the IE, IE-DC and IC-DC categories in $\widehat{\mathbf{M}}^{\Sigma}$ results based on the $f_{\delta\delta} = \pm 0.45$ threshold. Intermediate depth ($50 < z \leq 350$ km) bins for the deep-type slab regions are less consistent, due to a higher percentage (35%) of oblique mechanisms. Low values of $\|\widehat{\mathbf{M}}^{\Sigma}\|$ are common for these bins. For the shallow-type slabs the percentage of oblique mechanisms is similar to the results for deep bins, but there are also a number of bins showing compression where we expect extension, leading to a 34% disagreement with the IE category. Only five slab regions show 100% agreement with the Isacks and Molnar categories using both summation methods: the Hellenic, Halmahera, S. America and Scotia slabs. Of these, S. America-C is the only example of a deep-type slab region.

[25] We identify four distinct patterns in the summation results that cannot be incorporated into the Isacks and Molnar categories: First, some shallow-type slab regions show intermediate compression. This occurs with relatively homogeneous orientations for Calabria and Ryukyu-C, and somewhat less consistently for W. Philippines-N (Figure 5). In the case of the Ryukyu slab regions, along-strike changes in the focal mechanism orientations have been related to changes in the age of the subducting plate and the interaction of slab temperature changes with the 410 km phase change [cf. *Chen et al.*, 2004]. This distinct change in along-strike seafloor age is illustrated in Figure 1. However, a similar pattern of seafloor ages for Indonesia-W does not correlate with down-dip compression.

[26] Secondly, results in the uppermost $50 < z \leq 100$ km bin are nearly all classified as oblique or down-dip extensional. The oblique orientations mostly show a rotation of the tensors from the down-dip direction toward the slab-normal, which is indicative of an influence of slab bending. The lack of such rotations in the $100 < z \leq 150$ km bins imply that bending forces are not important there. The bending effect is also present in the modeling results shown in Figure 6.

[27] Thirdly, we observe in-plane rotations away from the down-dip axis of the slab that are consistent with depth for a

Figure 5. Average source mechanism tensor results for the 50 km depth bins that contain ≥3 CMTs for 34 of the 45 slab regions in Figure 1. Extensive orientation colors and gray circles adjacent to the beach balls follow the same convention as for Figure 4. Background colors for the slab labels indicate whether the slab is shallow or deep type. The background surrounding the beach balls can be one of four colors: light red indicating down-dip extension match to the Isacks and Molnar IE or IE-DC category, light blue indicating down-dip compression match to the Isacks and Molnar IC-DC category, light yellow indicating oblique orientations, and dark gray indicating compression or extension which cannot fit the Isacks and Molnar categories. For deep slabs, a black solid line indicates the estimated change from extension to compression based values of $f_{\delta\delta}$.

number of slab regions. This is most prominent for Tonga-C1, Izu-Bonin and Aleutian-W, as well as Kurile-N to some extent. Both Tonga-C1 and Izu-Bonin show distinct changes in the along-strike geometry, suggesting that surrounding mantle flow may be shearing the slab. The observation for the Aleutian-W. might lead us to relate this feature to oblique plate convergence, as illustrated by plate motion vectors in Figure 1. However, we do not find this in other

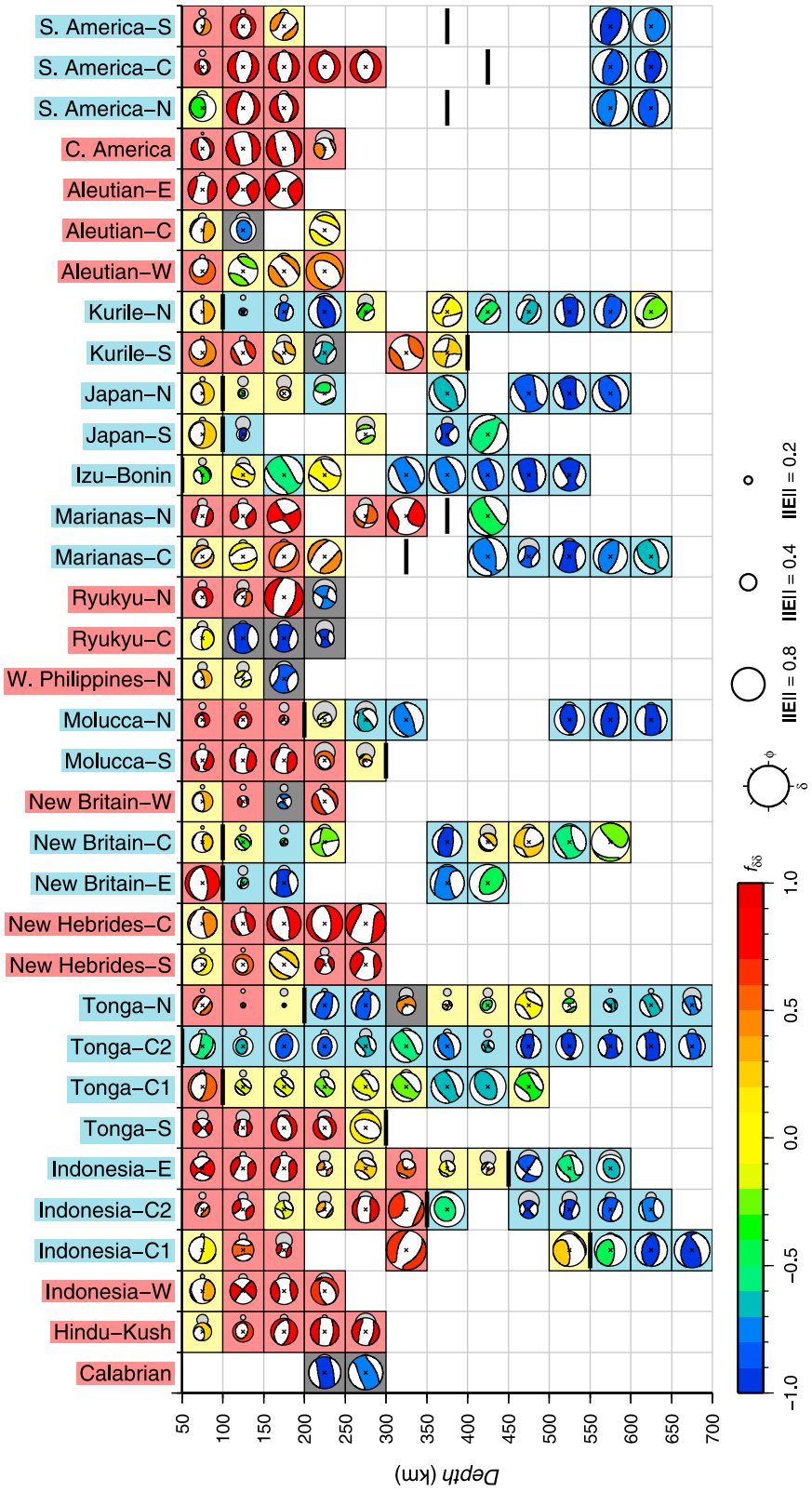

Figure 5

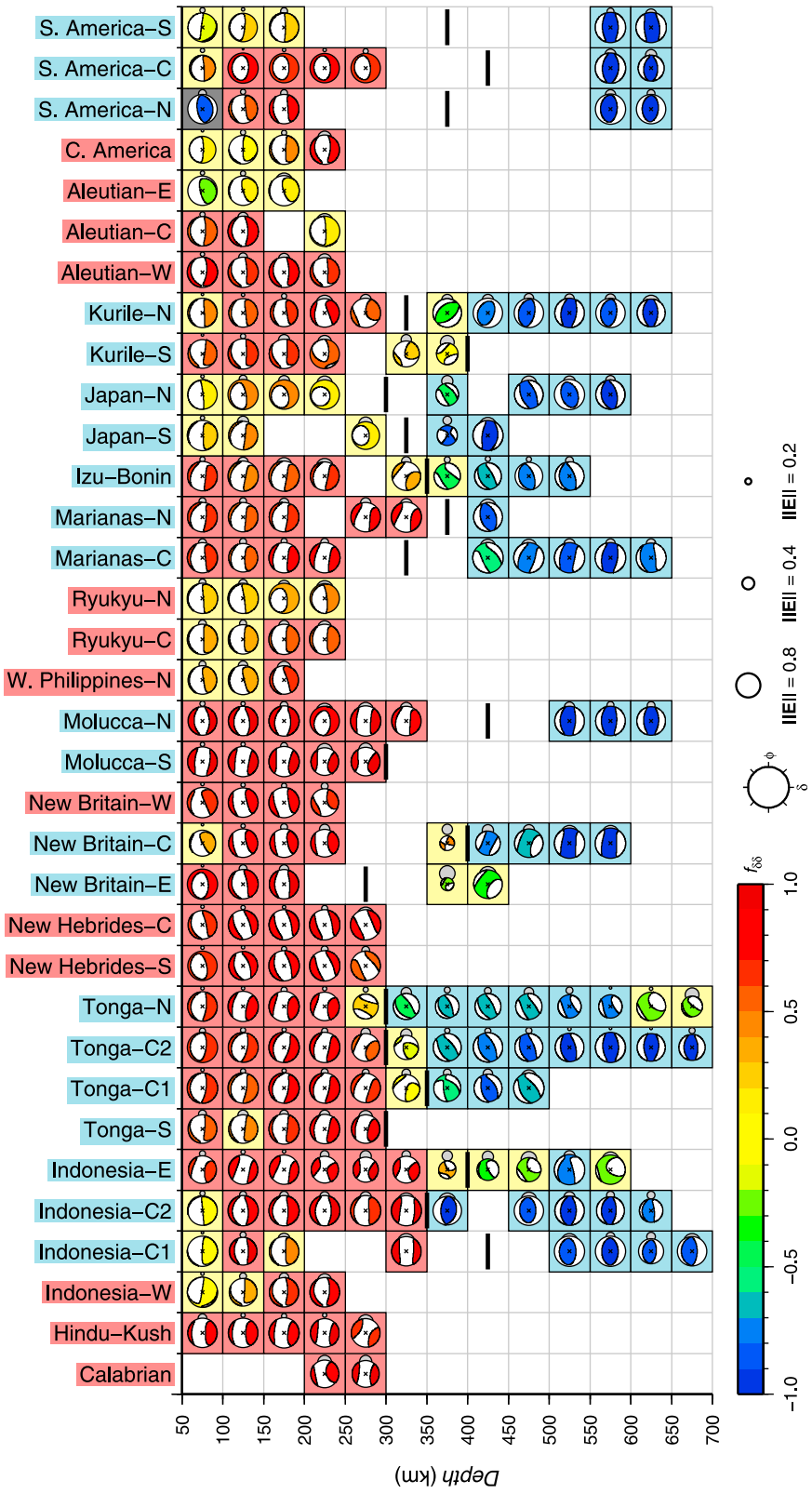

Figure 6. Average source mechanism tensors from numerical model stress tensors evaluated at the locations of CMTs used for Figure 5 (stiff slab case). The parameter setup of the model corresponds to the higher η slab (Table 1). The color scale and coordinate system follow that of data results in Figure 5, but the scaling of beach ball radii is reduced slightly due to greater homogeneity in the model results.

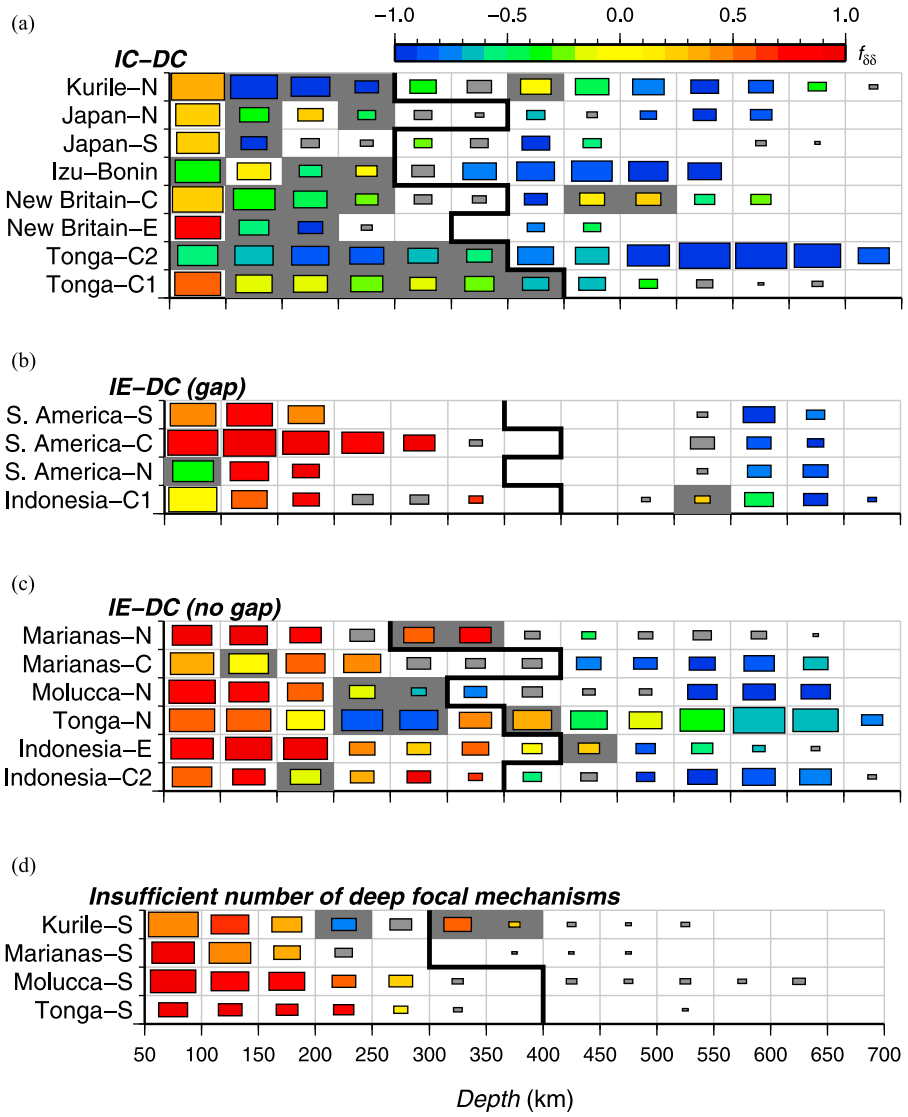

Figure 7. For the deep-type slab regions, comparison of predicted z_c from seismicity with $f_{\delta\delta}$ from the average source mechanism tensors. Rectangle colors show $f_{\delta\delta}$ for the $\widehat{\mathbf{M}}^{\Sigma}$ result in that bin (bins with no $\widehat{\mathbf{M}}^{\Sigma}$ result due to insufficient CMT data are colored gray). Based on the values of $f_{\delta\delta}$ (a) shows IC-DC slab regions, (b) shows IE-DC regions that have a clear seismicity gap, (c) shows IE-DC regions with no clear gap, and (d) shows regions with insufficient number of deep CMTs to make a judgment. Rectangle dimensions scale with the log number of hypocenters in each bin, and the thick black line shows z_c values estimated from the intermediate depth with lowest number of hypocenters. Bins where the value of $f_{\delta\delta}$ disagrees with the hypocenter number based estimate of z_c are highlighted with dark gray backgrounds.

regions where the plate motion is oblique to the slab-normal direction, such as Indonesia-W, New Hebrides and New Britain. Our modeling, which incorporates loading from the imposed plate motions, reproduces the rotations to some extent for the Izu-Bonin and Kurile-N slab regions.

[28] Fourthly, we find some clusters of oblique orientations that are not consistent between adjacent bins and also show heterogeneous CMT orientations within bins. This is observed for Indonesia-C2, Indonesia-E, Tonga-N, New Britain-C, and Japan-S/N, all of which are deep-type. Indonesia-C2 may be a special case since the subducting plate at the top of the slab is continental lithosphere. Heterogeneity for the Japan slab regions may relate to observations of distinct double-seismic zones with opposing focal mechanism orientations [e.g., *Igarashi et al.*, 2001; *Brudzinski et al.*, 2007]. The remaining three slab regions involve abrupt changes in the slab geometry, either along-strike or down-dip. Hence, it appears that a number of effects may lead to higher heterogeneity in the co-seismic deformation patterns of slabs.

3.3. Depth to Transition From Down-Dip Extension to Compression

[29] Out of 18 deep slabs with sufficient data $\widehat{\mathbf{M}}^{\Sigma}$, we find a distinct switch from intermediate extension to deep compression below 100 km in 10, fitting the IE-DC category

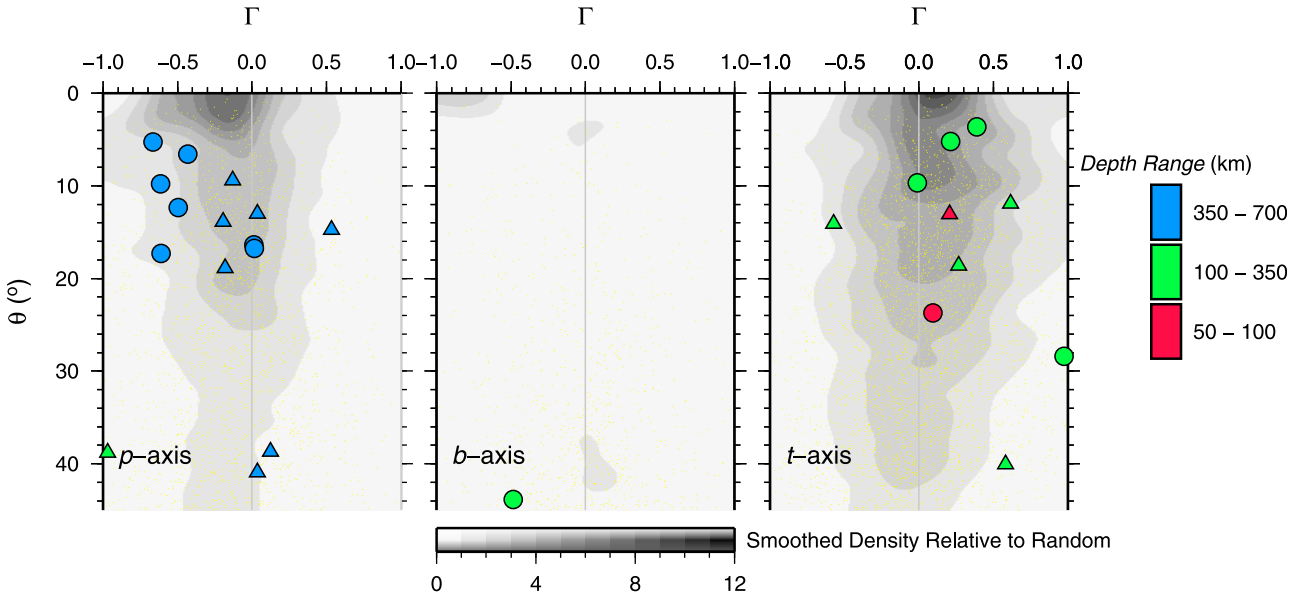

Figure 8. CLVD size as a function of orientation of the down-dip principal axis. Results for the individual CMTs are shown by yellow dots and background color, while results for the globally summed tensors in Figure 4 are shown by circles for $\widehat{\mathbf{M}}^{\Sigma}$ and triangles for $\mathbf{M}^{\Sigma}$ with colors bin depth range. The value of θ is the smallest angle between the P, T or B axis and the down-dip direction. Density of the points on each plot is computed on a 0.2 × 3° grid, multiplied by 1/sin(θ), smoothed using GMT surface [*Wessel and Smith*, 1998] then normalized by the maximum value, such that a uniform distribution of deviatoric moment tensor orientations would have a constant density.

(Figure 7). In the remaining eight, down-dip compression appears to dominate at all depths below 100 km (Figure 7a), though many of these results are categorized as oblique. The number of IE-DC types is larger for the $\mathbf{M}^{\Sigma}$ results (13/21) due to the influence of heterogeneity in some of the regions. For the regions that fit the IE-DC type, the depth of the switch from extension to compression, z_c, is generally consistent with gaps in the seismicity (Figure 7b). However, for slab regions where there is a minimum in the number of earthquakes as a function of depth, z_c is only sometimes consistent with the depth of that minimum (Figure 7c). For the Indonesian and S. American slab regions, as well as Marianas-C, the values of z_c estimated from $f_{\delta\delta}$ and from the number of earthquakes are consistent. However, for Molucca-N, Marianas-N and Kurile-S the z_c estimates are inconsistent by 100 km. In other IE-DC slab regions there are insufficient $\widehat{\mathbf{M}}^{\Sigma}$ results to test consistency of z_c estimates. Furthermore, the IC-DC slab regions sometimes show a distinct minimum in the number of earthquakes as a function of depth (e.g., New Britain and Japan-N). These inconsistencies are also observed for $\mathbf{M}^{\Sigma}$ where we consider more bins due to the requirement of just one CMT per bin. Hence, there is little evidence of a clear relation between the number of earthquakes and patterns of compression and extension in the slab. This is in part due to the lack of a common distribution shape for the number of earthquakes as a function of depth when comparing slabs globally.

3.4. CLVD Characteristics: Global Scale

[30] For individual CMTs in our catalog of slab associated earthquakes, we show that where $\theta < 30°$ for the P-axis there is a tendency for $\Gamma < 0$, and where $\theta < 30°$ for the T-axis there is a tendency for $\Gamma > 0$ (Figure 8). This may be summarized as a tendency toward the top-left and bottom-right example CMT orientations in Figure 3. These results are comparable to the observation of *Kuge and Kawakatsu* [1993] that the average CLVD component for CMTs in a slab relates to the ratio of in-plate compression to extension mechanisms. We find no general tendency toward positive or negative Γ where the B-axis is the closest axis to down-dip. Figure 8 shows the CLVD size and orientation relative to a uniform random distribution, indicating that CMTs are strongly clustered around either $\theta = 0°$ for either the P or T axis. However, the density at the edges of the plots (e.g., for the B-axis $\theta \approx 0$, $\Gamma \approx -0.8$) should be treated conservatively since the sparsity of data close to $\theta = 0°$ leads to greater uncertainty in the smoothing there.

[31] Overlaying results for the global depth bin summations indicates that CLVD components for $\widehat{\mathbf{M}}^{\Sigma}$ are larger than average CLVD components for the individual CMTs used to compute them. However, values of Γ for $\mathbf{M}^{\Sigma}$ results are smaller and generally consistent with the individual CMTs, as expected since they are dominated by individual CMTs. The pattern of negative Γ in tensors with P-axis $\theta < 30°$ is reflected in $\mathbf{M}^{\Sigma}$ and $\widehat{\mathbf{M}}^{\Sigma}$ for the $z > 350$ km bins, while the pattern of positive Γ in CMTs with T-axis $\theta < 30°$ is reflected in the $z \leq 350$ km bins.

3.5. CLVD Characteristics: Regional Scale

[32] For the average source mechanism tensor results in the binned slab regions, the relationship between Γ and θ is shown in Figure 9. We interpret these results with the caveat that strictly, the individual data points should not be treated equally since each point represents a different sized region

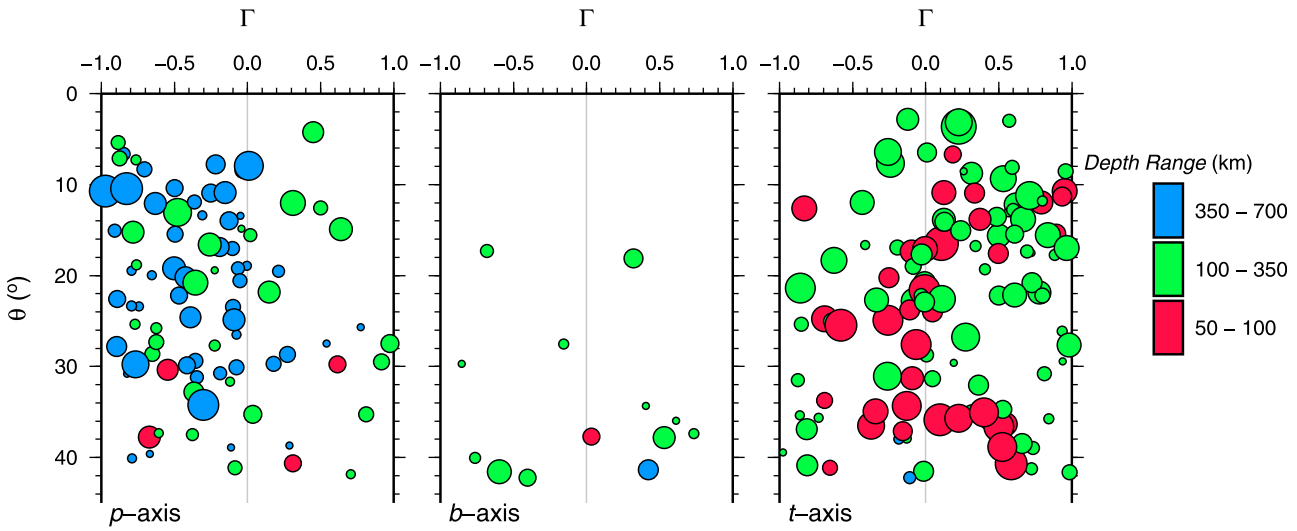

Figure 9. CLVD size as a function of orientation of the down-dip principal axis for the regionally binned $\widehat{\mathbf{M}}^{\Sigma}$ results, following the same convention as for Figure 8. Symbol sizes scale with the log of the number in each bin, and colors indicate the depth of the bin.

and a different number of CMTs. However, the separation into sub-regions allows us to examine the characteristics of co-seismic slab deformation with less bias toward slabs that have relatively higher numbers of CMTs (e.g., Tonga and S. America), and we account for the CMT number in each summation by varying point size. The same general patterns are observed as for the individual CMTs and global depth bins (Figure 8). However, a large amount of scatter with wide-ranging values of Γ is found at all values of θ, as well as generally larger values of $|\Gamma|$ than for the individual CMT data. When considering the results separated by depth range we find that nearly all deep bins lie in the $\Gamma < 0$ and P-axis $\theta < 30°$ region. In contrast, the down-dip compressional bins for the $50 < z \leq 100$ km and $100 < z \leq 350$ km depth ranges show several cases where $\Gamma > 0$. For the down-dip tensional bins (T-axis $\theta < 40°$) there is greater scatter in Γ than for the down-dip compressional bins. However, there is still a tendency for $\Gamma > 0$ when $0 \lesssim 20°$ for the T-axis. For the T-axis cases where $\theta > 30°$ there is a cluster of results in the $50 < z \leq 100$ depth range that corresponds to oblique orientations caused by slab bending.

3.6. Global Flow Model Comparisons

[33] Figures 10–12 summarize the modeling results for various parameter setups using the average of bin values of $f_{\delta\delta}$ and Γ, as well as average misfit to the CMT summed tensors using Θ^{DC} and $d\Gamma$. We separate the slab regions into the three Isacks and Molnar categories based first on whether the deepest contour is less than 350 km depth (IE), and based secondly on whether $z_c \leq 100$ km (IC-DC) or $z_c > 100$ km (IE-DC), where z_c is estimated from the CMT $\widehat{\mathbf{M}}^{\Sigma}$ results. A general result from the numerical modeling is that slabs are in extension for $z \lesssim 350$ km and compression below [*Alpert et al.*, 2010], showing a consistency with results from the IE and IE-DC regions (Figures 10 and 11). The down-dip compression at depth in the IC-DC and IE-DC categories appears as a direct response to the increase in viscosity for the lower mantle, illustrated by the lack of deep down-dip compression in the case where the viscosity contrast at the upper/lower mantle boundary is removed [cf. *Vassiliou and Hager*, 1988; *Alpert et al.*, 2010]. The down-dip extension at shallower depths appears as a combined response to the negative buoyancy and bending of the slab.

[34] The intermediate down-dip compression in the IC-DC category slab regions is not completely reproduced by any of the models (Figure 12). However, the two cases where slab stiffness is increased show a greater number of oblique results and deformation states closer to down-dip compression, illustrated by lower misfit values at intermediate depths ($100 < z \leq 250$ km) for the extra high viscosity slabs (Figure 12). This can be explained by a deeper influence of the plate motion associated shearing on slab stresses when the slabs are stiffer.

[35] In terms of Θ^{DC}, the control, weak asthenosphere and stiff slab models all show similar levels of misfit. Some of the best fits between summed tensor orientations are achieved in the uppermost $50 < z \leq 100$ km bin, except in the weak slab case, indicating that bending of the viscous slab does a good job in reproducing the orientations noted in section 3.1. Relatively high values of $\Theta^{DC}(\approx 70°)$ for the $250 < z \leq 350$ km range in the IE-DC category relate to the high variability in the orientations of the observed data. Although the misfit is roughly the same for all models, the predicted orientations for the various models are quite variable. This suggests a strong sensitivity of slab stresses to small changes in the slab rheology at these depths that could account for the variability in observed co-seismic deformation patterns.

[36] The CLVD characteristics for the model results generally follow the down-dip deformation state, such that average Γ values are negative and positive when average $f_{\delta\delta}$ values are negative and positive, respectively. This reproduces the CMT-based observations, as highlighted in Figures 8 and 9. There are two notable exceptions to this relation: First, in the $50 < z \leq 100$ km bins, where Γ values are generally close to zero. This corresponds to forces

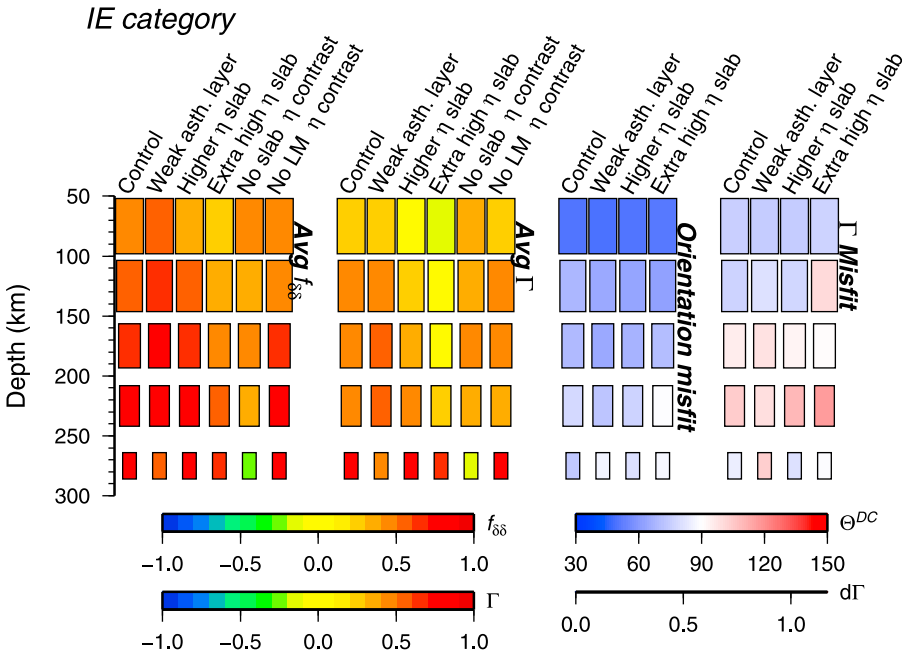

Figure 10. Model $\widehat{\mathbf{M}}^{\Sigma}$ results for the IE category slabs summarized in terms of average bin value of $f_{\delta\delta}$, average bin value of Γ, average orientation misfit (equation (5)) and average Γ misfit (equation (6)), considering each depth range separately. Rectangle sizes scale with the log of the total number of CMTs in all bins included in the averaging. In the case of misfit values, blue and red colors indicate misfit values respectively smaller and larger than those expected for a population of randomly oriented tensors.

dominated by the slab bending that are negligible in the along-strike direction. Secondly, for the IC-DC category where the slab viscosity is $1000\eta_{UM}$, showing a greater tendency toward negative Γ despite oblique values of $f_{\delta\delta}$. This occurs because the compressional stress due to forced plate velocities becomes so large that other stresses are negligible, and in the deviatoric stress tensor the stresses in perpendicular directions become extensive as a result.

[37] The fit to the relative CLVD magnitude, as quantified by $d\Gamma$ tends to be poor when fits to the orientation are also poor, which can be related to the positive correlation between Γ and $f_{\delta\delta}$. However, the reverse statement is not always true. We find that the Γ fits are poor where the Θ fits are reasonable for the $150 < z \leq 350$ km bins of the IE-DC and IE categories. Figure 10 shows that in the IE category the model predicts the largest CLVD components for the $150 < z \leq 350$ km bins but poor fits to the data. This results from a fairly homogeneous distribution of Γ in the model that does not reproduce the variation in observations illustrated by Figure 9. Otherwise, the model cases with $\eta_L = 10\eta_{LM}$ and $100\eta_{LM}$ show reasonable fits to the CLVD characteristics with depth. Notably, the increased number of oblique mechanisms for the extra stiff slab leads to a reduction in fit according to $d\Gamma$, especially in the IE-DC category.

4. Discussion

[38] As for previous analyses of intermediate to deep focal mechanism orientations [*Apperson and Frohlich*, 1987; *Chen et al.*, 2004], our results substantiate the main observation of *Isacks and Molnar* [1969], that slab earthquakes are dominantly characterized by down-dip compression or extension. Our results also refine the observations of *Kuge and Kawakatsu* [1993], that down-dip compression is associated with extensional intermediate co-seismic strain, and down-dip extension tends to associate with compressional intermediate co-seismic strain. In a global sense, co-seismic slab deformation can be described by down-dip extension with a positive CLVD component ($\Gamma > 0$) above ~350 km, and down-dip compression with a negative CLVD component below. This dominant pattern is correctly predicted by the numerical models of *Alpert et al.* [2010], where the key ingredients are the existence of slabs as viscosity and density anomalies, and a viscosity increase at $z = 660$ km. Global viscous deformation of slabs therefore provides the first physical model for the depth dependence of CLVD components in co-seismic deformation. The 660 km viscosity contrast is key to the development of down-dip compression [cf. *Vassiliou and Hager*, 1988] and extensive intermediate strain in the lower part of the slab, reproduced for a range of slab viscosities. Intermediate-depth extension results from a combination of the negative buoyancy of a dense slab pulling downward and the bending of a stiff slab. Compressive intermediate strain at intermediate depths can be explained either by a necking effect as weak slabs are stretched downward, by along-strike curvature of stiffer slabs, or by the interaction with toroidal flow around slab edges.

[39] We have disregarded quality restrictions in the selection of CMT data so as to maximize the spatial sampling of slabs. *Hjörleifsdóttir and Ekström* [2010] showed that CMT orientations should be fairly well constrained for shallower depth earthquakes, but did not focus on deeper earthquakes. The CLVD components of individual CMTs

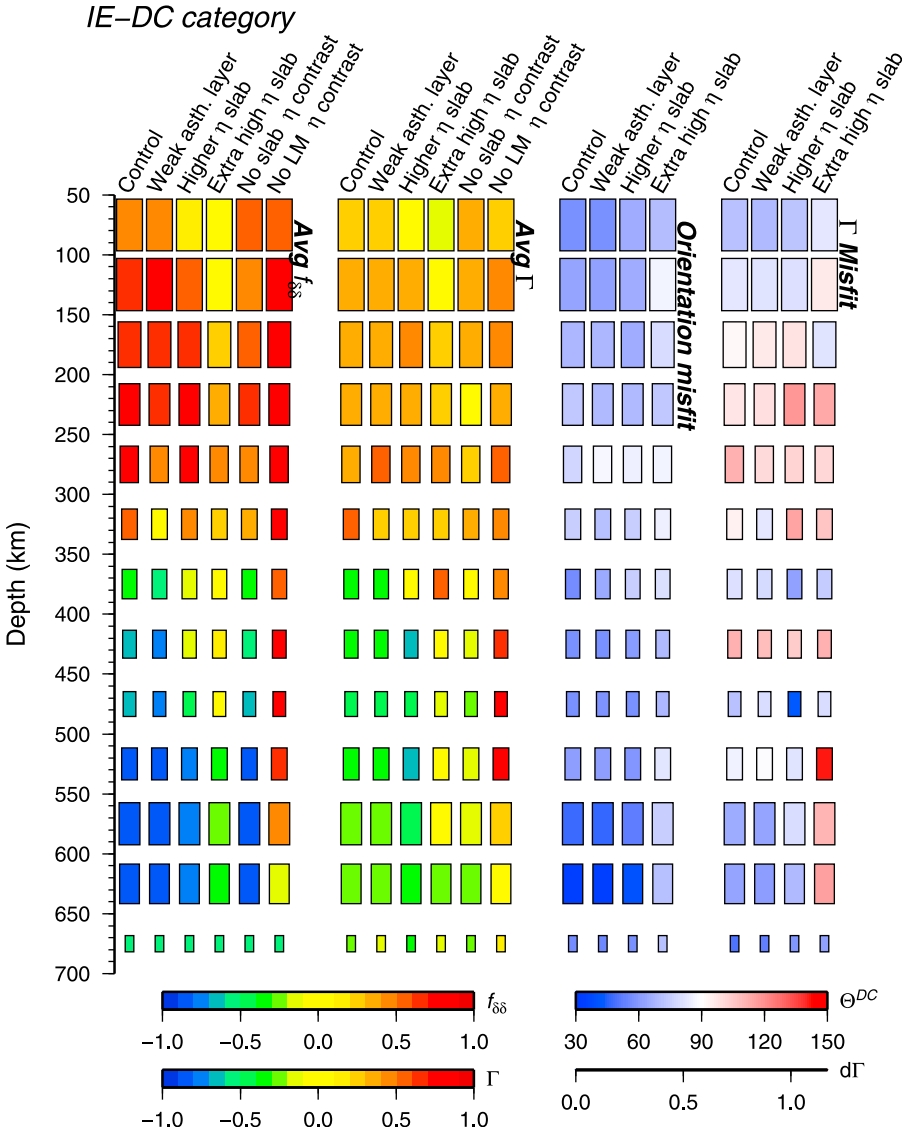

Figure 11. Model $\widehat{\mathbf{M}}^{\Sigma}$ results for the IE-DC category slabs summarized as in Figure 10.

can have strong uncertainties since they are dependent on constraining the smallest sized principal strain axes [e.g., *Frohlich*, 1995]. Here we show that the observations of *Kuge and Kawakatsu* [1993] persist in CLVD components of summed tensors, which represent the variation of better constrained P and T axes orientations of the CMTs.

[40] Considering the separation of slab regions into the Isacks and Molnar categories, the dominance of down-dip compression for deep ($z \geq 350$ km) earthquakes is the clearest pattern while results at intermediate depths ($50 < z \leq 350$ km) are more complicated. The tendency for either down-dip compression or extension at intermediate depths is greater than that predicted for a random model, but there are a large number of results that are oblique. Interpreting the oblique results purely based on the sign of the deformation, the slabs can broadly be divided into the Isacks and Molnar model categories of dominantly extensional, dominantly compressional or upper extension/lower compression. Unlike *Vassiliou and Hager* [1988], we find examples of down-dip compression throughout deep slabs in locations other than Tonga (e.g., Izu-Bonin, Kurile-N and New Britain-E). We also find examples of down-dip compression in slab regions that do not show seismicity at depth (Calabrian and Ryukyu-C slab regions), as noted in previous studies [e.g., *Isacks and Molnar*, 1971; *Kao and Chen*, 1991; *Bruno et al.*, 1999].

[41] In the case of the deeper slabs, *Vassiliou and Hager* [1988] found that compression was observed at shallower depths by plate forcing at the top of the slab, following the proposal by *Fujita and Kanamori* [1981] that compression is observed when subduction occurs at a faster rate than gravitational sinking. An analysis of summed CMT data by *Holt* [1995] for the Tonga slab shows that up to 60% of the relative plate motion may be absorbed by compression distributed along the slab as it is slowed by the 660 km viscosity contrast. Compression at intermediate depths is also generated by imposed plate velocities in the 3-D modeling of *Alpert et al.* [2010] when the slabs are relatively stiff, who noted that the northwesterly direction of net rotation for the Pacific in the NUVEL-HS3 model leads to

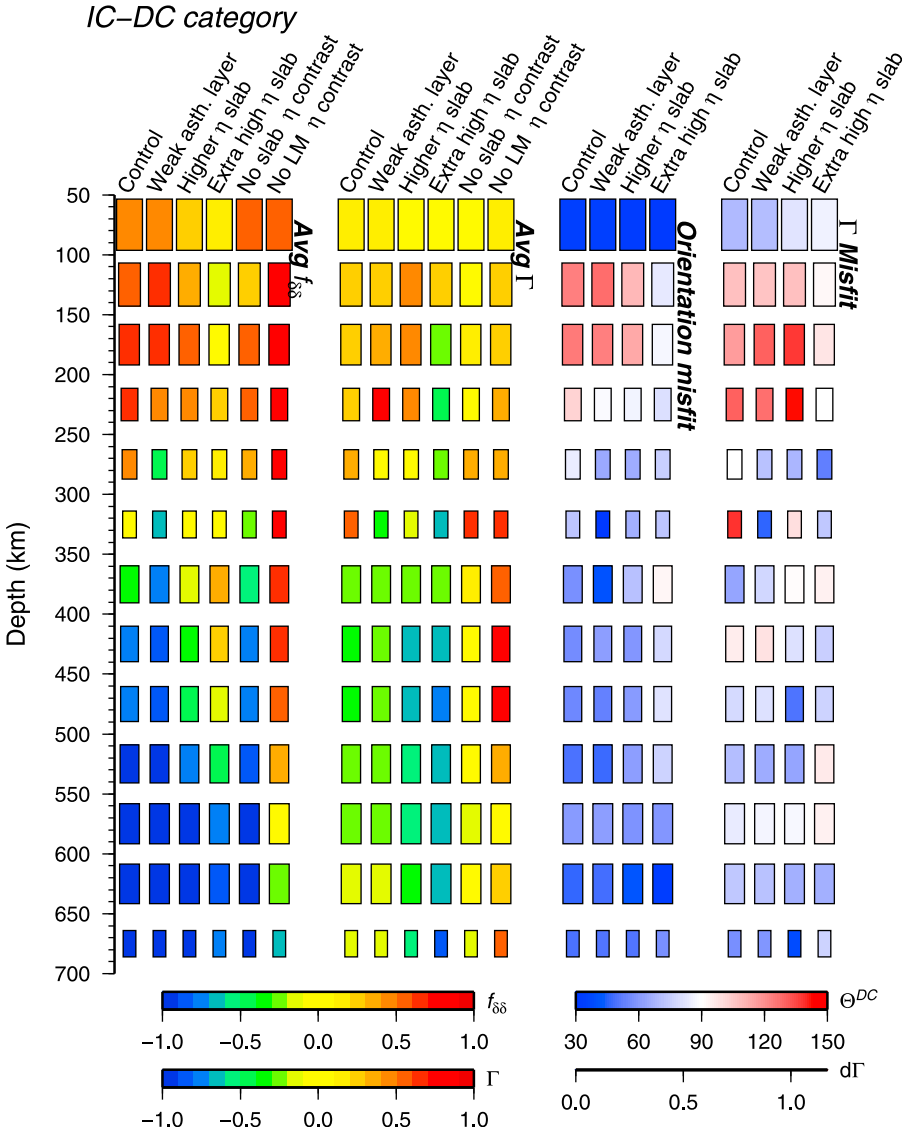

Figure 12. Model $\widehat{\mathbf{M}}^{\Sigma}$ results for the IC-DC category slabs summarized as in Figure 10.

enhanced intermediate compression in the west-dipping slabs such as Tonga and Kurile [cf. *Doglioni et al.*, 2007]. However, none of the cases show compression that is as closely aligned with the down-dip direction as in some of the data (e.g., Tonga-C2). This is because the plate motion direction is often oblique to the trench, leading to rotation of the model compressive axes away from the down-dip direction. Oblique orientations in the co-seismic deformation results indicate that oblique plate convergence is an important component of co-seismic slab deformation. However, the large model misfits where down-dip compression is observed suggest that other important mechanisms may not be incorporated. These mechanisms may become more apparent in models that can self-consistently generate realistic plate velocities as well as net rotations rather than having them imposed.

[42] In the case of the shallow-type slabs, down-dip compression is not reproduced in any of the modeling cases. Previous explanations for the Ryukyu slab [e.g., *Shiono et al.*, 1980; *Chen et al.*, 2004] suggest unique local features such that forces resisting the subduction are shallower than a upper/lower mantle viscosity contrast explaining compression for other slabs. The strong CLVD components and relative consistency of orientations suggest that this resistance occurs in much the same way as for the down-dip compression in deeper parts of other slabs. Hence, the compression may be interpreted as a regional change in the viscosity of the slab relative to the mantle below.

[43] Another aspect of our results related to the studies of *Isacks and Molnar* [1969, 1971] is the relation between the number of earthquakes with depth and the transition from extension to compression. In cases where there is a clear gap between intermediate and deep seismicity, we found a relation between the gap and this transition (e.g., Indonesia-C1, Marianas-C and all three S. America slab regions). However, in other cases there was no clear relation between the transition and the amount of seismicity with depth. This is partly due to a lack of similarity in the seismicity-depth profiles, making it difficult to objectively define a single turning point in number of earthquakes as a function of depth.

[44] *Vassiliou and Hager* [1988] interpreted the depth of a minimum in the number of earthquakes as a point at which the combined deviatoric stress due to the negative buoyancy and the collision with the viscous lower mantle is lowest. This can explain why the numerical modeling results presented here show compression/extension transitions that are more consistent with the seismicity-based estimates than the CMT-based estimates. We interpret the variation in histograms and observed depths of transition from extension to compression as reflecting the global heterogeneity in stress conditions affecting the $100 \leq z \leq 300$ km depth range for slabs that extend below $z = 350$ km. This limits the use of interpreting a single global distribution of seismicity with depth over this depth range, since there may be misinterpretations due to regional biases.

[45] Where mechanisms depart from the Isacks and Molnar categories due to oblique compression or extension, similar orientations over a range of depths suggest a shearing force applied to some slabs. These oblique orientations generally occur in the deep-type slabs and can be reproduced to some extent by the stiffer slab model results. In the models presented here, the shearing is a direct consequence of loading at the top of the slab by plate convergence oblique to the trench, which leads to essentially the same mantle shearing effect proposed for the Tonga slab by *Giardini and Woodhouse* [1986]. The rotation of P and T axes within the slab plane is consistent with the assertion of *Fujita and Kanamori* [1981] that slabs can be categorized by in-plane, rather than down-dip, compression or extension. An interesting case is the Aleutian slab, where, based plate motion (Figure 1), we would predict oblique convergence and orientations in the western slab region, as is observed. However, all of the model cases predict less obliqueness in the mechanism orientations than for the east. Seismic tomography results suggest that the slab extends far below the deepest seismicity in this region [e.g., *Engdahl and Gubbins*, 1987], yet the slab in our model is defined by the extent of seismicity. A deeper slab approaching the lower mantle may provide the resistive force necessary to generate the observed shear.

[46] The proportion of oblique mechanisms found in this study is greater than for previous results, which is likely to relate to our use of a more complete slab geometry. The observed rotation away from the slab coordinate system may indicate that the slab contours, as constrained by the hypocenter data, are unrepresentative of the true slab geometry and thus obliqueness is introduced by an incorrect rotation into the slab coordinate system. This is especially important in the $50 < z \leq 100$ km bin, where slab bending is better defined by a radius of curvature [e.g., *Wu et al.*, 2008; *Buffett and Heuret*, 2011] with constantly changing dip than by the flat triangular segments used in this study. However, the common rotation of the P and T axes for this depth range is consistent with that expected for slab bending and is reproduced by most models. Since the slab contours fit a smooth surface to the seismicity, they may also introduce errors into the rotation at locations close to where slab tears or breaks exist. However, there are also strong reasons to believe that the nature of deformation is no longer controlled by down-dip stresses close to strong geometrical changes at slab edges. Slabs that are stronger than the mantle induce toroidal flow around the edges [e.g., *Piromallo et al.*, 2006] that is likely to induce shear stresses. This effect leads to oblique orientations in the numerical modeling results presented here, especially where we observe oblique mechanisms and higher heterogeneity in the slab regions with sharp bends such as Indonesia-E and Tonga-N. Along strike changes in the slab geometry for the Izu-Bonin-Marianas slab regions [*Miller et al.*, 2004], Tonga and New Britain slabs are likely to be related to the observations of oblique orientations there. However, it is not clear that the oblique orientations are a direct result of forces from the bending rather than an effect of the changing reference frame of the slab coordinate system.

[47] *Frohlich* [1995] suggested that CLVD components in slab earthquakes could be explained in terms of down-dip and along-strike slab bends. By this mechanism, inward bending of a slab may lead to along-strike compression on the upper part where earthquakes occur, while outward bending would lead to along-strike extension. This may explain the intermediate depth $\Gamma > 0$ for the inward bending Indonesia-W and Molucca-S, $\Gamma < 0$ for the outward bending Japan-S and New Britain-E, and $\Gamma \approx 0$ in the relatively straight New Hebrides-C and S. American slabs. However, a similar relation is not observed for the inward bending Marianas-C, Caribbean and Halmahera, and relatively straight Indonesia-C1, C. America and Kurile-N. A difficulty in fully quantifying the role of geometrical changes in slabs on co-seismic slab deformation is the wide range in size and type of bends within the global slab population, from smooth arc shapes to sharp changes separating relatively straight sections, and the spatial distribution of earthquakes with relation to the bends.

[48] Summation results indicate a fairly high degree of heterogeneity in both orientation and CLVD components of the slab related earthquakes. We observe a greater scatter in the size of the CLVD component compared to *Kuge and Kawakatsu* [1993]. This is expected since we use relaxed quality restrictions, consider a wider range of slabs, and do not average our measures of CLVD or down-dip compression/extension in the same way. Some degree of heterogeneity will be related to uncertainties in the CMT calculations, but there is no strong reason for such uncertainty to show the same depth dependency as we find in the observed heterogeneity. Hence, we can interpret these variations in terms of heterogeneity of the stress-field and/or rheological properties of the slab. While heterogeneity in focal mechanism orientations may indicate a heterogeneous stress field within the slabs, a wide range of CMT orientations are possible for a single stress tensor [*McKenzie*, 1969]. Nevertheless, heterogeneous stress at the intermediate depths where we observe greater focal mechanism heterogeneity could be related to double seismic zones at the same depths [e.g., *Frohlich*, 2006; *Brudzinski et al.*, 2007]. This is especially relevant for the Kurile-N, Japan-N and New Britain slabs, where opposing focal mechanism orientations have been observed for the separate zones [*Brudzinski et al.*, 2007]. The localized deformation into such zones is unlikely to be captured in the numerical models which highlight a smoothly varying stress field related to viscous flow, and may explain why the heterogeneity is greater in the observational results. However, the compilations of double seismic zone results by *Frohlich* [2006] and *Brudzinski et al.* [2007], as well as examination

of focal mechanism orientations within bins used here, indicate little generality to co-seismic strain patterns for such zones. Hence, the most we can infer is that their occurrence in the same depth range and the localization of seismicity may relate to our observed focal mechanism heterogeneity. We also consider it likely that variations in slab rheology play an important role in the observed heterogeneity.

[49] Since earthquakes are a brittle process their occurrence requires an elastic component to slab rheologies, yet in this study we interpret the co-seismic deformation in terms of stresses in viscous slabs and therefore implicitly assume a heterogeneous slab rheology. The earthquakes tend to occur in spatial clusters within the slabs (see Figure 2) and it is likely that the slab rheology has some degree of spatial heterogeneity (e.g., adjacent weak and strong patches). This may include the reactivation of remnant faults, as suggested by *Jiao et al.* [2000]. In the numerical modeling results, the stress orientations are most sensitive to changes in viscosity parameters at the depths (~200–350 km) where we observe the highest levels of focal mechanism heterogeneity. Hence, it is likely that a heterogeneous slab rheology has its strongest effect on focal mechanism heterogeneity in the same depth range.

5. Conclusions

[50] The categories of slab deformation suggested by *Isacks and Molnar* [1971], i.e., intermediate extension, intermediate extension - deep compression, and intermediate to deep compression, are generally consistent with our analysis of an increased data set and better constrained slab geometries. However, many slabs show obliquely oriented P and T axes. Departure from the Isacks and Molnar categories can be related to bending of the top of the slab, oblique plate convergence leading to a shearing force within the slab, and a heterogeneous stress field which we ascribe to spatially heterogeneous or mechanically anisotropic rheological properties. The depth of transition from extension to compression can be related to gaps in seismicity but otherwise does not reflect seismicity patterns in a clear manner. This can be interpreted as a sensitivity of the transition to minor changes in the slab stress conditions or mechanical properties, which are most heterogeneous in the $100 \leq z \leq 350$ km depth range. From the CLVD components of the summed tensor results, we find a tendency for compressional intermediate strain when the slab is down-dip extensional, and extensional intermediate strain when the slab is down-dip compressional. This is observed for both individual CMTs, summations of CMTs and summations of normalized CMTs, substantiating the observations of *Kuge and Kawakatsu* [1993]. Those CLVD patterns are predicted successfully by global mantle flow models with viscous slabs that extend in response to gravity and compress as they approach a viscosity increase from the upper to lower mantle. First order, general properties of observed slab deformation can therefore be described by a purely viscous representation, while a more complete understanding requires more detailed consideration of the sensitivity to local properties of the slab and the surrounding mantle, particularly in the 200–300 km depth range.

[51] **Acknowledgments.** We thank Hitoshi Kawakatsu for comments on an earlier draft of the manuscript, as well as Cliff Frohlich, an anonymous reviewer and editor Tom Parsons for valuable reviews and suggestions. The numerical modeling results presented here made use of the CitcomS code which is made available via the Computational Infrastructure for Geodynamics (www.geodynamics.org). We also made use of the Approximate Nearest Neighbor library [*Arya et al.*, 1998]. Figures were produced using the GMT software [*Wessel and Smith*, 1998]. The study was partially supported by NSF grants EAR-0643365 and EAR-0930046.

References

Alisic, L., M. Gurnis, G. Stadler, C. Burstedde, L. C. Wilcox, and O. Ghattas (2010), Slab stress and strain rate as constraints on global mantle flow, *Geophys. Res. Lett.*, *37*, L22308, doi:10.1029/2010GL045312.

Alpert, L. A., T. W. Becker, and I. W. Bailey (2010), Global slab deformation and centroid moment tensor constraints on viscosity, *Geochem. Geophys. Geosyst.*, *11*, Q12006, doi:10.1029/2010GC003301.

Amelung, F., and G. King (1997), Large-scale tectonic deformation inferred from small earthquakes, *Nature* , *386*, 702–705.

Apperson, K. D., and C. Frohlich (1987), The relationship between Wadati-Benioff zone geometry and P, T and B axes of intermediate and deep focus earthquakes, *J. Geophys. Res.*, *92*(B13), 13,821–13,831, doi:10.1029/JB092iB13p13821.

Arya, S., D. M. Mount, N. S. Netanyahu, R. Silverman, and A. Y. Wu (1998), An optimal algorithm for approximate nearest neighbor searching fixed dimensions, *J. ACM*, *45*(6), 891–923.

Astiz, L., T. Lay, and H. Kanamori (1988), Large intermediate-depth earthquakes and the subduction process, *Phys. Earth Planet. Inter.*, *53*(1–2), 80–166.

Bailey, I. W., T. W. Becker, and Y. Ben-Zion (2009), Patterns of coseismic strain computed from southern California focal mechanisms, *Geophys. J. Int.*, *177*, 1015–1036, doi:10.1111/j.1365-246X.2009.04090.x.

Bailey, I. W., Y. Ben-Zion, T. W. Becker, and M. Holschneider (2010), Quantifying focal mechanism heterogeneity for fault zones in central and southern California, *Geophys. J. Int.*, *183*(1), 433–450, doi:10.1111/j.1365-246X.2010.04745.x.

Becker, T. W. (2006), On the effect of temperature and strain-rate dependent viscosity on global mantle flow, net rotation, and plate-driving forces, *Geophys. J. Int.*, *167*(2), 943–957, doi:10.1111/j.1365-246X.2006.03172.x.

Billen, M. I., and M. Gurnis (2003), Comparison of dynamic flow models for the central aleutian and tonga-kermadec subduction zones, *Geochem. Geophys. Geosyst.*, *4*(4), 1035, doi:10.1029/2001GC000295.

Brudzinski, M. R., and W. P. Chen (2005), Earthquakes and strain in subhorizontal slabs, *J. Geophys. Res.*, *110*, B08303, doi:10.1029/2004JB003470.

Brudzinski, M. R., C. H. Thurber, B. R. Hacker, and E. R. Engdahl (2007), Global prevalence of double Benioff zones, *Science*, *316*(5830), 1472–1474, doi:10.1126/science.1139204.

Bruno, G., I. Guerra, A. Moretti, and G. Neri (1999), Space variations of stress along the Tyrrhenian Wadati-Benioff zone, *Pure Appl. Geophys.*, *156*(4), 667–688, doi:10.1007/s000240050318.

Buffett, B. A., and A. Heuret (2011), Curvature of subducted lithosphere from earthquake locations in the Wadati-Benioff zone, *Geochem. Geophys. Geosyst.*, *12*, Q06010, doi:10.1029/2011GC003570.

Chen, P. F., C. R. Bina, and E. A. Okal (2004), A global survey of stress orientations in subducting slabs as revealed by intermediate-depth earthquakes, *Geophys. J. Int.*, *159*(2), 721–733, doi:10.1111/j.1365-246X.2004.02450.x.

Conrad, C. P., and M. D. Behn (2010), Constraints on lithosphere net rotation and asthenospheric viscosity from global mantle flow models and seismic anisotropy, *Geochem. Geophys. Geosyst.*, *11*, Q05W05, doi:10.1029/2009GC002970.

Conrad, C. P., and C. Lithgow-Bertelloni (2004), The temporal evolution of plate driving forces: Importance of slab suction versus slab pull during the cenozoic, *J. Geophys. Res.*, *109*, B10407, doi:10.1029/2004JB002991.

Doglioni, C., E. Carminati, M. Cuffaro, and D. Scrocca (2007), Subduction kinematics and dynamic constraints, *Earth Sci. Rev.*, *83*(3-4), 125–175, doi:10.1016/j.earscirev.2007/04.001.

Dziewonski, A. M., and J. H. Woodhouse (1983), An experiment in systematic study of global seismicity: Centroid-moment tensor solutions for 201 moderate and large earthquakes of 1981, *J. Geophys. Res.*, *88*(B4), 3247–3271, doi:10.1029/JB088iB04p03247.

Dziewonski, A. M., T. A. Chou, and J. H. Woodhouse (1981), Determination of earthquake source parameters from waveform data for studies of global and regional seismicity, *J. Geophys. Res.*, *86*(B4), 2825–2852, doi:10.1029/JB086iB04p02825.

Ekström, G. (2007), Global seismicity: Results from systematic waveform analyses, 1976–2005, in *Treatise on Geophysics*, vol. 4, edited by G. Schubert, pp. 473–481, Elsevier, New York.

Engdahl, E. R., and D. Gubbins (1987), Simultaneous travel time inversion for earthquake location and subduction zone structure in the central

Aleutian Islands, *J. Geophys. Res.*, *92*(B13), 13,855–13,862, doi:10.1029/JB092iB13p13855.
Engdahl, E. R., and C. H. Scholz (1977), A double Benioff zone beneath the central Aleutians: An unbending of the lithosphere, *Geophys. Res. Lett.*, *4*(10), 473–476, doi:10.1029/GL004i010p00473.
Engdahl, E. R., R. van der Hilst, and R. Buland (1998), Global teleseismic earthquake relocation with improved travel times and procedures for depth determination, *Bull. Seismol. Soc. Am.*, *88*(3), 722–743.
Forsyth, D. W., and S. Uyeda (1975), On the relative importance of the driving forces of plate motions, *Geophys. J. R. Astron. Soc.*, *43*, 163–200.
Frohlich, C. (1995), Characteristics of well-determined non-double-couple earthquakes in the Harvard CMT catalog, *Phys. Earth Planet. Inter.*, *91*(4), 213–228, doi:10.1016/0031-9201(95)03031-Q.
Frohlich, C. (2006), *Deep Earthquakes*, Cambridge Univ. Press, Cambridge, U. K.
Frohlich, C., and K. D. Apperson (1992), Earthquake focal mechanisms, moment tensors, and the consistency of seismic activity near plate boundaries, *Tectonics*, *11*(2), 279–296.
Fujita, K., and H. Kanamori (1981), Double seismic zones and stresses of intermediate depth earthquakes, *Geophys. J. R. Astron. Soc.*, *66*(1), 131–156.
Giardini, D. (1984), Systematic analysis of deep seismicity: 200 centroid-moment tensor solutions for earthquakes between 1977 and 1980, *Geophys. J. R. Astron. Soc.*, *77*(3), 883–914.
Giardini, D., and J. H. Woodhouse (1986), Horizontal shear flow in the mantle beneath the Tonga arc, *Nature*, *319*, 551–555, doi:10.1038/319551a0.
Gripp, A. E., and R. G. Gordon (2002), Young tracks of hotspots and current plate velocities, *Geophys. J. Int.*, *150*(2), 321–361.
Gudmundsson, O., and M. Sambridge (1998), A regionalized upper mantle (RUM) seismic model, *J. Geophys. Res.*, *103*, 7121–7136.
Hanks, T. C., and H. Kanamori (1979), A moment magnitude scale, *J. Geophys. Res.*, *84*, 2348–2350.
Hjörleifsdóttir, V., and G. Ekström (2010), Effects of three-dimensional earth structure on CMT earthquake parameters, *Phys. Earth Planet. Inter.*, *179*(3-4), 178–190, doi:10.1016/j.pepi.2009.11.003.
Holt, W. E. (1995), Flow fields within the Tonga slab determined from the moment tensors of deep earthquakes, *Geophys. Res. Lett.*, *22*(8), 989–992, doi:10.1029/95GL00786.
Igarashi, T., T. Matsuzawa, N. Umino, and A. Hasegawa (2001), Spatial distribution of focal mechanisms for interplate and intraplate earthquakes associated with the subducting Pacific plate beneath the northeastern Japan arc: A triple-planed deep seismic zone, *J. Geophys. Res.*, *106*(B2), 2177–2191, doi:10.1029/2000JB900386.
Isacks, B., and P. Molnar (1969), Mantle earthquake mechanisms and the sinking of the lithosphere, *Nature*, *223*(5211), 1121–1124.
Isacks, B., and P. Molnar (1971), Distribution of stresses in the descending lithosphere from a global survey of focal-mechanism solutions of mantle earthquakes, *Rev. Geophys.*, *9*(1), 103–174.
Isacks, B., J. Oliver, and L. R. Sykes (1968), Seismology and the new global tectonics, *J. Geophys. Res.*, *73*(18), 5855–5899.
Jiao, W., P. G. Silver, Y. Fei, and C. T. Prewitt (2000), Do intermediate- and deep-focus earthquakes occur on preexisting weak zones? An examination of the Tonga subduction zone, *J. Geophys. Res.*, *105*, 28,125–28,138, doi:10.1029/2000JB900314.
Julian, B. R., A. D. Miller, and G. R. Foulger (1998), Non-double-couple earthquakes: 1. Theory, *Rev. Geophys.*, *36*, 525–550, doi:10.1029/98RG00716.
Kagan, Y. Y. (2009), On geometric complexity of earthquake focal zone and fault system: A statistical study, *Phys. Earth Planet. Inter.*, *173*, 254–268, doi:10.1016/j.pepi.2009.01.006.
Kao, H., and W. P. Chen (1991), Earthquakes along the Ryukyu-Kyushu arc: Strain segmentation, lateral compression, and the thermomechanical state of the plate interface, *J. Geophys. Res.*, *96*(B13), 21,443–21,485, doi:10.1029/91JB02164.
Knopoff, L., and M. J. Randall (1970), The compensated linear vector dipole: A possible mechanism for deep earthquakes, *J. Geophys. Res.*, *75*, 4957–4963.
Kostrov, B. V. (1974), Seismic moment and energy of earthquakes and seismic flow of rock, *Phys. Solid Earth*, *1*, 23–40.
Kuge, K., and H. Kawakatsu (1993), Significance of non-double couple components of deep and intermediate-depth earthquakes: Implications from moment tensor inversions of long-period seismic waves, *Phys. Earth Planet. Inter.*, *75*(4), 243–266, doi:10.1016/0031-9201(93)90004-S.
McKenzie, D. P. (1969), The relation between fault plane solutions for earthquakes and the directions of the principal stresses, *Bull. Seismol. Soc. Am.*, *59*(2), 591–601.
Miller, M. S., B. L. N. Kennett, and G. S. Lister (2004), Imaging changes in morphology, geometry, and physical properties of the subducting Pacific plate along the Izu-Bonin-Mariana arc, *Earth Planet. Sci. Lett.*, *224*(3–4), 363–370, doi:10.1016/j.epsl.2004.05.018.
Müller, R. D., M. Sdrolias, C. Gaina, and W. R. Roest (2008), Age, spreading rates, and spreading asymmetry of the world's ocean crust, *Geochem. Geophys. Geosyst.*, *9*, Q04006, doi:10.1029/2007GC001743.
Piromallo, C., T. W. Becker, F. Funiciello, and C. Faccenna (2006), Three-dimensional instantaneous mantle flow induced by subduction, *Geophys. Res. Lett.*, *33*, L08304, doi:10.1029/2005GL025390.
Riedesel, M., and T. H. Jordan (1989), Display and assessment of seismic moment tensors, *Bull. Seismol. Soc. Am.*, *79*(1), 85–100.
Shiono, K., T. Mikumo, and Y. Ishikawa (1980), Tectonics of the Kyushu-Ryukyu arc as evidenced from seismicity and focal mechanism of shallow to intermediate-depth earthquakes, *J. Phys. Earth*, *28*(1), 17–43.
Sykes, L. R. (1966), The seismicity and deep structure of island arcs, *J. Geophys. Res.*, *71*(12), 2981–3006.
Vassiliou, M. S., and B. H. Hager (1988), Subduction zone earthquakes and stress in slabs, *Pure Appl. Geophys.*, *128*(3), 547–624, doi:10.1007/BF00874550.
Wessel, P., and W. H. F. Smith (1998), New, improved version of the Generic Mapping Tools released, *Eos Trans. AGU*, *79*(47), 579.
Wu, B., C. P. Conrad, A. Heuret, C. Lithgow-Bertelloni, and S. Lallemand (2008), Reconciling strong slab pull and weak plate bending: The plate motion constraint on the strength of mantle slabs, *Earth Planet. Sci. Lett.*, *272*(1–2), 412–421, doi:10.1016/j.epsl.2008.05.009.
Zhong, S. (2001), Role of ocean-continent contrast and continental keels on plate motion, net rotation of lithosphere, and the geoid, *J. Geophys. Res.*, *106*, 703–712.
Zhong, S., M. Zuber, L. Moresi, and M. Gurnis (2000), Role of temperature-dependent viscosity and surface plates in spherical shell models of mantle convection, *J. Geophys. Res.*, *105*(B5), 11,063–11,082, doi:10.1029/2000JB900003.

L. A. Alpert, I. W. Bailey, T. W. Becker, and M. S. Miller, Department of Earth Sciences, University of Southern California, Los Angeles, CA 90089, USA. (iainbailey@gmail.com)